TAT-RasGAP 317-326 kills cells by targeting inner-leaflet–enriched phospholipids

Marc Serulla, Gabriel Ichim, Filip Stojceski, Gianvito Grasso, Sergii Afonin, Mathieu Heulot, Tim Schober, Robyn Roth, Cédric Godefroy, Pierre-Emmanuel Milhiet, et al.

TAT-RasGAP$_{317-326}$ kills cells by targeting inner leaflet-enriched phospholipids

Marc Serulla[1], Gabriel Ichim[2*], Filip Stojceski[3*], Gianvito Grasso[3], Sergii Afonin[4], Tim Schober[5], Robyn Roth[6], Cédric Godefroy[7], Pierre-Emmanuel Milhiet[7], Kushal Das[8], Ana Garcia Saez[8], Andrea Danani[3], and Christian Widmann[1]

[1]Department of Biomedical Sciences, University of Lausanne, Rue du Bugnon 7, 1005 Lausanne, Switzerland

[2]Center for Research on Cancer of Lyon (CRCL), LabEX DEVweCAN, University of Lyon, Rue Laennec 28, 69008 Lyon, France

[3] Dalle Molle Institute for Artificial Intelligence (IDSIA), Scuola Universitaria Professionale della Svizzera italiana (SUPSI), Università della Svizzera italiana (USI), Centro Galleria 2, 6928 Manno, Switzerland

[4]Institute of Biological Interfaces (IBG-2), Karlsruhe Institute of Technology (KIT) POB 3640, 76021 Karlsruhe,Germany

[5]Institute of Organic Chemistry (IOC), KIT, Fritz-Haber-Weg 6, 76131 Karlsruhe,Germany

[6]Washington University Center for Cellular Imaging, Washington University School of Medicine, South Euclid Ave 660, 63110 St. Louis, MO, United States

[7]Centre de Biochimie Structurale (CBS), CNRS, INSERM, University Montpellier, Rue de Navacelles 29, 34090 Montpellier, France

[8]Interfaculty Institute of Biochemistry, Eberhard Karls University Tübingen, Hoppe-Seyler-Strasse 4, 72076 Tübingen, Germany

*, equal contribution

Address correspondence: Christian Widmann, Department of Biomedical Sciences, Rue du Bugnon 7, 1005 Lausanne, Switzerland, Phone: +41 21 692 5123, Fax: +41 21 692 5505, E-mail: Christian.Widmann@unil.ch.

Keywords: cell-penetrating peptides, anticancer peptides, membranolytic peptide, phosphatidylserine, phosphoinositides, necrotic cell death.

Contribution

Conception and design of study: MS and CW
Acquisition of data: MS, GI, FS, GG, SA, TS, RR, PM, and KD
Analysis and/or interpretation of data: MS, GI, FS, GG, SA, TS, RR, PM, and CW
Drafting the manuscript: MS, GI, FS, GG, PM, SA, TS, RR, and CW
Revising the manuscript and approval of the submitted version: all authors

Abstract

TAT-RasGAP$_{317-326}$ is a cell-penetrating peptide (CPP)-based construct with anticancer and antimicrobial activities. This peptide kills a subset of cancer cells in a manner that does not involve known programmed cell death pathways. Here we have elucidated the mode of action allowing TAT-RasGAP$_{317-326}$ to kill cells. The peptide translocates into the cytosol, where it binds lipids such as phosphatidylinositol-bisphosphate (PIP_2) and phosphatidylserine (PS) that are enriched in the inner leaflet of the plasma membrane. This binding leads to plasma membrane disruption and cell death. Decreasing the amounts of PIP_2 in cells renders them more resistant to the peptide. The W317A TAT-RasGAP$_{317-326}$ point mutant, known to have impaired killing activities, has reduced abilities to bind PIP_2 and PS and is less able than the wild-type peptide to translocate through biomembranes, presumably because of a higher propensity to adopt an α-helical state. This work shows that TAT-RasGAP$_{317-326}$ kills cells via a form of necrosis that relies on the physical disruption of the plasma membrane once the peptide targets specific phospholipids found on the cytosolic side of the plasma membrane.

Introduction

Most current anticancer therapies trigger genetically encoded regulated cell death pathways to achieve disease control. Manipulation of these pathways can be very efficacious in cancer chemotherapies, as exemplified by the recent development of drugs, such as Venetoclax, targeting intrinsic apoptosis-regulating Bcl2 protein family members that can cure patients of chronic lymphocytic leukemia [1]. However, cancer cells, through alterations in cell death pathways, can become refractory to chemotherapeutic-induced death leading to relapses [2, 3]. Strategies that trigger non-genetically encoded forms of cell death would provide additional therapeutic options to fight cancers.

TAT-RasGAP$_{317-326}$ is a chimeric peptide composed of a cell-penetrating sequence (G^{48}RKKRRQRRR^{57}) from the human immunodeficiency virus (HIV) transactivator of transcription (TAT) protein, and a ten amino acid sequence (W^{317}MWVTNLRTD^{326}) derived from the Src homology 3 (SH3) domain of p120 RasGAP (Ras GTPase activating protein) [4]. This construct has several anticancer properties, including inhibition of metastatic progression and tumor cell sensitization to anticancer therapies [4-6]. TAT-RasGAP$_{317-326}$ was shown to sensitize tumor xenografts in mice to chemotherapy and radiotherapy with no apparent toxicity to healthy tissues [7, 8]. This peptide also displays broad antimicrobial activities [9].

TAT-RasGAP$_{317-326}$ can also directly kill a subset of cancer cell lines in a manner that is distinct from apoptosis, necroptosis, parthanatos, pyroptosis, and autophagy [9]. This peptide appears, therefore, to harbor killing properties that may be difficult for cancer cells to alleviate through resistance-building alterations within known regulated cell death pathways. The mechanisms used by TAT-RasGAP$_{317-326}$ to kill cells have

eluded detailed characterization as up to now. In the present study, we provide experimental evidence that this peptide induces a necrotic-like form of death by targeting phospholipids enriched in the inner leaflet of the plasma membrane.

Results

Preferential binding of TAT-RasGAP$_{317-326}$ to inner leaflet phospholipids

Electron microscopy (EM) visualization of HeLa cells incubated with TAT-RasGAP$_{317-326}$ demonstrate that they can experience gross membrane disruption without any indication of forming pores such as those seen upon incubation with the streptolysin O hemolytic exotoxin (Figure S1). The peptide is therefore unable to form large pores but we cannot exclude that it creates small and/or transient pores that escape detection by EM. The EM data are also compatible with the possibility that the peptide directly targets plasma membrane components to disrupt cell integrity without forming pore-like structures. To assess if TAT-RasGAP$_{317-326}$ has a specific selectivity for individual plasma membrane phospholipids, multilamellar vesicles (MLVs) made of various phospholipid compositions were incubated with a fluorescent version of the peptide. As negative controls, the TAT CPP alone was used, as well as a single amino acid substitution (W317A) mutant of the TAT-RasGAP$_{317-326}$ peptide. This mutant has impaired anticancer properties [10, 11]. Even though its ability to be taken up by cells is lower compared to the wild-type peptide (Figure S2A), when taken up to similar extent (Figure S2B), the mutant peptide is far less potent in killing cells in comparison to the wild-type peptide (Figure S2C). In short-term incubation settings, the W317A mutant peptide was unable to induce cell death (Figure S2D).

The lipids used in this study are listed in Table 1. Table 2 provides the composition of the cytosolic (“inner”) and extracellular (“outer”) leaflets of the plasma membrane that we have considered in the present work. Figure 1 shows that TAT-RasGAP$_{317-326}$ and control peptides could not bind to liposomes made of lipids equally present in both leaflets of the plasma membrane such as phosphatidylcholine (PC),

phosphatidylethanolamine (PE) or cholesterol (CHL). Similar results were obtained when these peptides were incubated with lipids typically present in the outer leaflet of the plasma membrane like GM1 and GM3 gangliosides or sphingomyelin (SM). On the other hand, TAT-RasGAP$_{317-326}$ bound to inner leaflet-enriched phosphatidylinositol(4,5)bisphosphate [PI(4,5)P_2] and phosphatidylserine (PS) more avidly than control peptides. Other lipids present in the inner leaflet of the plasma membrane did either not interact with TAT-RasGAP$_{317-326}$ (e.g. phosphatidylinositol) or displayed no specificity for the wild-type peptide (e.g. phosphatidic acid). Cardiolipin, a mitochondria-specific phospholipid, when present at a 10% concentration in liposomes, interacted stronger with TAT-RasGAP$_{317-326}$ compared to the control peptides. The specificity of this binding was lost when the level of cardiolipin in liposomes rose to 20%, which is the physiological concentration of this lipid in the inner mitochondrial membrane. Overall, TAT-RasGAP$_{317-326}$ had a much higher affinity for vesicles the lipid composition of which mimicked the inner plasma membrane leaflet compared to bilayers made of outer membrane leaflet-specific lipids. Our data suggest that TAT-RasGAP$_{317-326}$ display a specific tropism for bisphosphorylated phosphoinositides, such as PI(4,5)P_2 and PI(3,5)P_2, and to a lower extend to PI(3,4)P_2. Mono-phosphate phosphoinositides like PI(3)P interacted very poorly with the peptides. There was no specific binding of the wild-type peptide to PI(3,4,5)P_3, which suggests that the affinities observed here are not purely based on the larger net negative charge of the cationic peptide-targeted lipid species. We also note that in almost all cases, the W317A mutant demonstrated binding preferences similar to the TAT-only control, suggesting a more substantial impact of the RasGAP moiety of TAT-RasGAP$_{317-326}$, rather than its TAT part, in the binding-specifying peptide-lipid interactions. The data from Figure 1 indicate overall that TAT-RasGAP$_{317-326}$ interacts

strongly with specific phospholipids enriched in the cytosolic side of the plasma membrane and to cardiolipin.

TAT-RasGAP$_{317-326}$ kills cells in a mitochondria-independent manner

The observation that TAT-RasGAP$_{317-326}$ possesses a high affinity to cardiolipin suggests a mitochondria involvement in the peptide-mediated cell death. However, lipid bilayers containing 10% cardiolipin, the concentration at which specificity of binding of the wild-type peptide versus the control peptides was observed (see Figure 1), were not markedly permeabilized by TAT-RasGAP$_{317-326}$ (Figure 2A). Even though high cardiolipin concentration (20%)-containing vesicles could be permeabilized by wild-type TAT-RasGAP$_{317-326}$ to some extent (Figure S3), it appears that cardiolipin is, in fact, a rather protective phospholipid against TAT-RasGAP$_{317-326}$-induced permeabilization as PC-containing vesicles are less lysed when they contain cardiolipin (compare Figure S3 and Figure S4). Removing mitochondria from HeLa cells (Figure 2B-C), while preventing mitochondria-dependent cell death, did not render them resistant to TAT-RasGAP$_{317-326}$-induced death (Figure 2D). Hence, even though the peptide can bind to cardiolipin-containing membranes, this interaction does not appear to mediate the ability of the peptide to kill cells.

TAT-RasGAP$_{317-326}$ permeabilizes membranes made of inner leaflet phospholipids

As shown above, TAT-RasGAP$_{317-326}$ preferentially binds phospholipids enriched in the inner leaflet of the plasma membrane, such as phosphatidylserine and

bisphosphorylated phosphoinositides. To determine if such binding underlies the ability of the peptide to permeabilize membranes, giant unilamellar vesicles (GUVs) made of various phospholipids were incubated with TAT-RasGAP$_{317-326}$ and control peptide, and their membrane integrity was evaluated through calcein intake (Figure 3). GUVs containing either PI(4,5)P_2 or PS were efficiently permeabilized by TAT-RasGAP$_{317-326}$ but not (in the case of PS) or inefficiently [in the case of PI(4,5)P_2] by the mutant W317A peptide. Similar results were obtained with other bisphosphorylated phosphoinositides such as PI(3,4)P_2 and PI(3,5)P_2 (Figure S5). Additionally, GUVs with outer membrane-like composition were not significantly permeabilized by the peptides. In contrast, GUVs made of inner membrane-enriched phospholipids were very efficiently permeabilized by TAT-RasGAP$_{317-326}$. The control TAT-RasGAP$_{317-326}$(W317A) peptide was about ten-fold less efficient in permeabilizing these GUVs compared to the wild-type peptide (Figure 3).

We next investigated by atomic force microscopy the impact of TAT-RasGAP$_{317-326}$ on lipid bilayers made of inner leaflet lipids. Figure S6 shows that the wild-type peptide, but not the W317A mutant version, effectively destabilized such bilayers in a detergent like-manner rather than through the formation of discrete structures like pores. These data suggest that TAT-RasGAP$_{317-326}$ tropism for inner leaflet-enriched phospholipids mediates its ability to disrupt membrane integrity in a detergent-like manner.

PI(4,5)P_2 plasma membrane depletion impairs TAT-RasGAP$_{317-326}$-induced cell death

Lipid binding and GUV permeabilization experiments indicate that TAT-RasGAP$_{317-326}$ induces cell death by direct permeabilization of the plasma membrane through binding

to phospholipids like PI(4,5)P_2. Depleting this phospholipid from the inner layer of the plasma membrane should, therefore, hamper TAT-RasGAP$_{317-326}$ from killing cells. We tested this assumption by inducing the translocation to the plasma membrane of an enzyme able to dephosphorylate the inositol ring of phosphoinositides at position 5 (Figure 4A-B), thereby diminishing the levels of PI(4,5)P_2 as assessed by decreased recruitment of PI(4,5)P_2-binding proteins to the plasma membrane (Figure 4C). This treatment lowered the ability of the peptide to permeabilize cells (Figure 4D) without affecting its uptake (Figure 4E). These data support the notion that TAT-RasGAP$_{317-326}$ kills cells through binding to specific phospholipids of the inner layer of the plasma membrane after reaching the cytosol.

TAT-RasGAP$_{317-326}$ membranolytic activity is antagonized by the ESCRT machinery

Plasma membrane damage triggers a healing response through removal of damaged areas by endocytosis or via exosome shedding. The endosomal sorting complex required for transport (ESCRT) machinery has recently been shown to participate in such membrane repair events [12, 13]. If TAT-RasGAP$_{317-326}$ has membranolytic activities through its ability to target inner leaflet phospholipids as indicated by the results shown above, it can be foreseen that the ESCRT machinery antagonizes the killing activity of the peptide. To assess this hypothesis, dominant-negative CHMP3$^{1-179}$ and VPS4A^{E228Q}, core members of the ESCRTIII complex, and the ESCRT disassembly sub-complex, respectively, were expressed in HeLa using a doxycycline-inducible system (Figure 5A). This manipulation sensitized cells to TAT-RasGAP$_{317-326}$-induced death (Figure 5B). In the case of CHMP3$_{1-179}$, the sensitization could be

partly explained by an increase in peptide uptake (Figure 5C, middle panel). However, VPS4A^{E228Q} expression in cells did not affect peptide uptake (Figure 5C, right panel) while still protecting cells from TAT-RasGAP$_{317-326}$ (Figure 5B, right panel). These data are therefore compatible with the notion that the ESCRT machinery can repair TAT-RasGAP$_{317-326}$-induced membrane damage and protect cells from its lytic activity.

The W317A mutation promotes helicity in RasGAP$_{317-326}$, affecting peptide-membrane interaction

To assess if the diminished specific lipid binding capacity of W317A results from a secondary structure distinct from the one adopted by TAT-RasGAP$_{317-326}$, the peptide structures and peptide-membrane interactions were studied by molecular modeling, circular dichroism (CD), and solid-state nuclear magnetic resonance spectroscopy (ssNMR). Simulation experiments were performed with TAT-RasGAP$_{317-326}$ and the W317A mutant in the presence of lipid bilayers of variable compositions. The *in silico* experiments were performed using atomistic unbiased simulations in order to study the peptides interfacial interactions with phospholipidic bilayers [14] and how the latter influence the conformational transitions of the peptides. In the membrane-bound states, the propensity of TAT-RasGAP$_{317-326}$ to adopt an α-helical structure within the RasGAP moiety was very low, in sharp contrast to the W317A mutant, regardless of the lipid composition of the model bilayers (Figure 6). The observed helicity of the TAT moiety was barely affected by the W317A mutation. This indicates that a tryptophan at position 317 is a potent α-helix disruptor within the RasGAP sequence of TAT-RasGAP$_{317-326}$.

The different conformations of the two bound peptides translated into differential, but still lipid composition-independent, modes of membrane insertion (Figure 7). The less structured wild-type peptide was found to insert slightly deeper into membranes compared to the W317A mutant (Figure 7A). This was not only due to its larger hydrophobicity, but also to a higher likelihood of amino acids around the W317 residue to contact lipids of the inner leaflet-like membrane (Figure 7B). Furthermore, the TAT segment of the wild-type peptide appeared to “attacks” the membrane with a sharper angle than the W317A mutant (Figure 7C) but without significant modulation of the overall probability to contact the lipids (Figure 7B). This set of data indicates that a tryptophan residue at position 317 hampers α-helix formation in the RasGAP$_{317\text{-}326}$ segment of the peptide. Compared to the W317A mutant, this provides TAT-RasGAP$_{317\text{-}326}$ with a better angle of membrane insertion, increases its flexibility and rises its capacity to contact inner layer membrane phospholipids. These differences may explain the lower membranolytic activity of the W317A mutant compared to the parental TAT-RasGAP$_{317\text{-}326}$ peptide.

Circular dichroism experiments, comparing the conformations of the wild-type and the W317A peptides in the presence of membrane mimetics, provided additional evidence that the W317A mutation impacts the peptide’s conformation (Figure S7). At identical concentrations, we observed more intense CD signals or more pronounced spectral features associated with folding for the W317A peptide. For instance, in the helix-promoting TFE (2,2,2-trifluoroethanol) the mutant peptide showed a more typical α–helix since the $\pi \rightarrow \pi^*_{\parallel}$ transition was occurring at the canonical 208 nm wavelength and the (PE/PA) ratio (Figure S7A) was close to 2:1 (Figure S7B). In the same environment, the wild-type peptide displayed a left-shifted $\pi \rightarrow \pi^*_{\parallel}$ transition and a PE/PA ratio of 1. However, while the W317A substitution favored helicity, it did not

affect the overall peptide conformational plasticity. Indeed, the spectra of TAT-RasGAP$_{317-326}$ and its W317A mutant were similar in aqueous or 1:1 TFE:PB (phosphate buffer) environments, as well as in the presence of the zwitterionic detergent dodecylphosphocholine (DPC) or in negatively charged *lyso*-phosphatidylglycerol (oPG) micelles (Figure S7B). Finally, in negatively charged dodecylsulfate (SDS) micelles, TAT-RasGAP$_{317-326}$ folded to a more β-like conformation as judged by the pronounced n→π* transition at 196 nm with a turn-like geometry contribution since the parallel π→π* transition occurred after 220 nm instead of at the classical 217-218 nm wavelength.

Negative curvature may facilitate peptide translocation through membrane [15], while positive curvature may trigger lipid packing defects and membrane disruption [16]. We used ^{31}P ssNMR to investigate potential differences between TAT-RasGAP$_{317-326}$ and its W317A mutant in membrane curvature modulation. Specifically, we studied the temperatures (T_{L-H}) at which lamellar (L) to inverted hexagonal (H_{II}) lipid phase transition (Figure S8A) occurred in PE-based membranes reconstituted with the two peptides (Figure S8B). In pure PE membranes, TAT-RasGAP$_{317-326}$ promoted negative curvature since the H_{II} phase was already detected at the lowest tested temperature (5°C). The L to H_{II} phase transition nominally occurs between 15° and 20° in untreated membranes. In contrast, the W317A mutant peptide favored positive curvature (Figure S8B). As the outer membrane leaflet is globally composed of neutral phospholipids, like in the model PE bilayer used here, this could mechanistically explain the reduced ability of the W317A mutant to enter cells (see Figure S2). In PE membranes loaded with negatively charged lipids (PS and PG), an environment closer to what is found in the inner layer of the plasma membrane, the wild-type peptide lost its negative membrane curving abilities and gained positive membrane curving properties (Figure

278 S8B). The increased propensity to induce positive membrane curvature on inner layer-
279 like membranes may be part of the mechanism used by TAT-RasGAP$_{317-326}$ to
280 destabilize membranes. The difference in L to H_{II} phase transition-inducing properties
281 observed between the two peptides in PE membranes disappeared upon addition of
282 anionic lipids. This is compatible with the notion that TAT-RasGAP$_{317-326}$ ended up
283 more concentrated than its mutant in the vicinity of the membrane due to stronger
284 affinities for negatively charged phospholipids (see Figure 1).

285

Discussion

TAT-RasGAP$_{317-326}$ has been reported earlier to kill cells using a non-regulated necrotic-like death pathway [10]. The present work provides the molecular characterization of this pathway, which is schematically described in Figure 8. TAT-RasGAP$_{317-326}$ needs to enter cells by direct translocation through the plasma membrane to exert its biological activity [17]. Once in the cytoplasm, the peptide remains in the membrane vicinity where it targets anionic phospholipids, such as PI(4,5)P_2 and PS, which are enriched in the inner layer of the plasma membrane. This interaction destabilizes the plasma membrane, compromising its integrity and ultimately leading to a necrotic type of cell death. In addition, this study also gives an explanation to why the substitution of the tryptophan at position 317 for an alanine residue in TAT-RasGAP$_{317-327}$ profoundly decreases the ability of the peptide to enter and kill cells.

Distinct uptake efficiencies between the wild-type and the mutant peptides are not explained by differences in peptide-lipid interaction since both peptides interact similarly - and rather inefficaciously - with outer membrane lipids (Figure 1). Rather, it may be the higher ability of the wild-type peptide to promote negative curvature in zwitterionic membranes such as the outer membrane that could facilitate peptide entry (Figure S8).

Once inside cells, the killing ability of the peptides is modulated by peptide-membrane interplay. TAT-RasGAP$_{317-327}$, but not the W317A mutant, efficiently interacts with anionic lipids such as PI(4,5)P_2, PS, or cardiolipin. This cannot be explained by global differences in electrostatic interactions between the peptides and the membrane as both wild-type and mutant peptides carry the same net positive charges (+9). The two

peptides do not share the same secondary structures however, the W317A substitution strongly favoring α helix formation in the RasGAP moiety. This is likely an important determinant for the membranolytic activity of TAT-RasGAP$_{317-326}$. For instance, compared to the W317A mutant, the less structured wild-type peptide “attacks” membranes with sharper angle allowing deeper insertion in the lipid core. In addition, in comparison to alanine, a tryptophan residue at position 317 increases the ability of the surrounding amino acids to move closer to lipids (Figure 7). Finally, in the presence of anionic lipids, wild-type TAT-RasGAP$_{317-326}$ gains the ability to induce positive membrane curvature, while the mutant peptide on this matter behaves identically in all membranes tested (Figure S8). This can be interpreted as the wild-type peptide binding more avidly to anionic membranes compared to the mutant peptide, facilitating membrane disruption. The “rigidity” of the W317A peptide weakens the interactions with lipid membranes containing anionic lipids, flattens the angle of action, and diminishes peptide-lipid interaction. This could mechanistically explain the reduced biological activity of the W317A mutant.

TAT-RasGAP$_{317-326}$ displays binding preferences for certain, but not all, anionic lipids. For example, the peptide binds phosphoinositide biphosphate better than phosphoinositide mono- or tri- phosphate. In addition, TAT-RasGAP$_{317-326}$ membrane destabilizing activity is affected differently by negatively charged lipids. For example, cardiolipin vesicles, which allow efficient TAT-RasGAP$_{317-326}$ binding, are not well permeabilized. As mentioned above, these phenomena cannot be explained by just simple electrostatic interactions but rather, as suggested by others [18], by the lipid and membrane topology, which might be critical determinant modulating peptide-lipid binding and peptide membranolytic or sensitizing activity.

The plasma membrane damage induced by TAT-RasGAP$_{317-326}$ can be repaired, at least to a certain extent, by the ESCRT machinery as the inhibition of the latter sensitizes cells to the peptide (Figure 5). This suggests that cells tolerate a certain amount of TAT-RasGAP$_{317-326}$-induced plasma membrane damage because they can engage membrane repair pathways such as the one triggered by the ESCRT machinery. Only when the membrane repair capacity of the cells is overwhelmed by high enough concentrations of cytosolic TAT-RasGAP$_{317-326}$ will cells undergo necrosis. Since TAT-RasGAP$_{317-326}$ induces a non-regulated necrotic type of death, cells do not have the possibility to develop a resistance based on mutations in elements of programmed cell death pathways. However, they might still acquire resistance through altering membrane lipid composition, mutations of genes participating in the making of specific elements of the plasma membrane or upregulating the cell's ability to repair its plasma membrane.

A number of cationic cell-penetrating peptides have shown interesting anticancer properties, including their ability to deliver drugs into cells, and through intrinsic anti-metastatic, anti-angiogenic, and apoptosis potentiating properties. However, only a limited subset of cell-penetrating peptides display substantial membranolytic activities [19, 20]. It appears that among them, only NAD1 (*Nicotiana alata Defensin 1*) disrupts the plasma membrane of cells through interaction with PI($_{4.5}$)P$_2$ [21] leading to effective plasma membrane disruption in a mechanism comparable to the one described here for TAT-RasGAP$_{317-326}$.

In conclusion, membrane active peptides like TAT-RasGAP$_{317-327}$ or NAD1 trigger direct membrane disruption resulting in cell death through a mechanism that is not mediated by cell-encoded proteins (in contrast to apoptosis or necroptosis, for

example). This mechanism relies on the binding of the peptide to specific phospholipids enriched in the inner layer of the plasma membrane. Presumably, cells cannot easily counteract such non-genetically encoded death pathways through mutations, unless they upregulate membrane repair pathways using the ESCRT machinery for example. Therefore, TAT-RasGAP$_{317-327}$- and related compound-based therapies could be used against tumors that do not respond to canonical treatments.

Materials and methods

Chemicals

Streptolysin O (SLO) (#S5265, Sigma-Aldrich) was resuspended in water (25'000-50'000 units/ml), aliquoted and stored at -80°C. Before use, SLO was activated with 10 mM DTT (dithiothreitol) for 30 min at 37°C, then diluted to 50-100 units/ml in PBS (phosphate buffered saline) supplemented with 1 mM $MgCl_2$ and used immediately. One unit corresponds to the dose that causes 50% lysis of 2% red blood cell suspensions in PBS, pH 7.4, after a 30 min incubation at 37°C. Glutaraldehyde 25% (#G5882, Sigma-Aldrich) was diluted to 2% in 100 mM NaCl, 30 mM HEPES (4-(2-hydroxyethyl)-1-piperazineethanesulfonic acid) [pH7.2], 2 mM $MgCl_2$, 150 mM sucrose and aliquoted at -20°C. Propidium iodide (#81845 or #P4170, Sigma-Aldrich) was aliquoted (400 µg/ml) in water and kept at -20°C. HEPES, Triton X 100, DMSO (dimethyl sulfoxide), NP40 (IGEPAL CA-630), chloroform, and sucrose were from Sigma-Aldrich (#H4034, #9002-93-1, #D2660, #I3021, #319988, and #S0389, respectively). NaCl from Flasher Chemical (#7647-14-5), $MgCl_2$ from Eurobio (#018023). 0.05% Trypsin-EDTA (ethylenediaminetetraacetic acid) was from Gibco (#25300-054). Trypan blue (0.4%) (Life Technologies, #15250061) was dissolved with PBS to final concentration (0.2%) and stored at room temperature. Rapamycin (Life Technologies, #PHZ1235, lot #1951776A,) was dissolved in DMSO (200 µM stock solution) and kept at -20°C. Calcein (Sigma-Aldrich, #C0875) was resuspended in PBS (80 mM stock solution) and kept at -20°C. Methanol was from Reactolab SA (#99046). DAPI (4′,6-diamidino-2-phenylindole) (ThermoFisher, #D1306) was dissolved in water to a final concentration of 5 mg/ml and stored at -20°C. PBS was from Laboratorium Dr.G.BICHSEL (#1000324). Actinomycin D was from Calbiochem (#114666) and

ABT737 from ApexBIO (#A8193). TFE was from Carl Roth (#71729). Protease inhibitor and phosphatase inhibitors were from Roche (#04693116001 and #04906837001, respectively) and were used following the manufacturer's instructions. Tris-HCl was from Merck (#101675948). Puromycin 10 mg/ml was diluted in 20 mM HEPES buffer (pH 6.2–6.8) (ThermoFisher, #A1113802).

Antibodies

Primary antibodies. The anti-cytochrome *c* (rabbit) and the anti-β-actin (mouse) antibodies were from Cell Signaling (#11940 and #4970, respectively), the anti-HA (human influenza hemagglutinin) (YPYDVPDYA) mouse antibody was from Biolegend (#MMS-101R) and the anti-vinculin mouse antibody was from Sigma-Aldrich (#V9131)

Secondary antibodies. The goat anti-mouse and anti-rabbit HRP (horseradish peroxidase) conjugate antibodies were from Bio-Rad (#170-6516 and #170-6515, respectively). The goat anti-rabbit and anti-mouse Alexa Fluor 680 conjugated antibodies were from Invitrogen (#A21109 and #A21057, respectively).

Peptides

Non-fluorescent peptides were synthesized in a retro-inverso manner (i.e. synthesized with D-amino acids in the opposite direction compared to the natural sequence). *i)* *TAT-RasGAP$_{317–326}$* The TAT moiety corresponds to amino acids 48–57 of the HIV TAT protein (RRRQRRKKRG) and the RasGAP$_{317–326}$ moiety corresponds to amino acids 317–326 of the human p120 RasGAP protein (DTRLNTVWMW). These two moieties are separated by two glycine linker residues. *ii)* *W317A*. Compared to the parental

peptide, TAT-RasGAP$_{317-326}$ (W317A), also named W317A, has an alanine instead of a tryptophan at position 317 (DTRLNTVWMA). The FITC-labelled (fluorescein isothiocyanate) peptides were synthesized in an inverso manner (i.e. with D-amino acids but in the direction corresponding to the natural sequence), except for FITC-TAT that is a retro-inverso peptide. The FITC dye was conjugated at the N-terminus of the peptides using aminocaproic acid as a linker. All peptides were synthesized by SBS Genetech CO, (Beijing, China).

Cells

Raji cells, HeLa cells, HeLa cells stably expressing a yellow fluorescent protein (YFP)-tagged Parkin [22], and HeLa cells bearing a doxycycline-inducible system to express CHMP3$^{1-179}$ or VPS4A^{E228Q} [13] were cultured in RPMI (#61870, Invitrogen). In the case of HeLa CHMP3$^{1-179}$ or VPS4A^{E228Q}, the cell culture was complemented with 4 µg/ml of puromycin every 3 days. All culture media were supplemented with 10% heat-inactivated fetal bovine serum (FBS) (#10270-106, Invitrogen) and cells were cultured in 5% CO_2, 37°C incubators. Cells were cultured in RPMI for experimental purposes except for HeLa cells in Figure 5 that were incubated in DMEM (#61965, Invitrogen). In both cases supplemented with 10% heat inactivated fetal bovine serum.

Calcium phosphate transient transfection

Calcium phosphate-based transfection of HeLa cells was performed as previously described [23].

Plasmids

Plasmid hLyn[1-11]-hMTOR[2021-2113]-HA-mRFP-T2A-hFKBP1A-Inp54p (#1014) was a gift from Peter Varnai (Addgene plasmid PM-FRB-mRFP-T2A-FKBP-5-ptase, #40896; http://n2t.net/addgene:40896; RRID:Addgene_40896). Plasmid PH-PLCD1[1-170]-GFP (#1027) was a gift from Tamas Balla (Addgene plasmid # 51407; http://n2t.net/addgene:51407 ; RRID:Addgene_51407).

Peptide uptake measurement

Cells were incubated for one hour with the indicated concentrations of FITC-labelled peptides. Adherent cells were washed with 500 µl of PBS, incubated with trypsin for 10 min at 37°C, collected with 1 ml of RPMI or DMEM (Figure 5) containing 10% FBS and centrifuged for 3 min at 192 g at 4°C. Floating cells were pelleted by a 3 minute centrifugation at 192 g at 4°C. Pelleted cells were resuspended in 500 µl PBS or 0.2% trypan blue when indicated. Peptide uptake was measured by flow cytometry using a FC 500 Beckman Coulter apparatus (Figure S2) or a Cytoflex S Beckman Coulter apparatus (all other figures). Data analysis was done with the Kaluza version 1.3 software (Beckman Coulter) or the Cytexpert software (Beckman Coulter).

Cell death measurement

Raji cells (Figure S2). The cells were seeded in 24 well plates (Costar, 3526) in 10% FBS-containing RPMI medium. Cells were then treated as indicated in the figures, collected and centrifuged for 3 min at 192 g at 4°C. The cells were resuspended in 500 µl PBS. The samples were transferred to cytometer tubes (Sarstedt, 55.1759) and analyzed by flow cytometry (FC-500, Beckman Coulter). Cell death was assessed by the gain in cell complexity (SSC channel). Data analysis was done with the Kaluza Version 1.3 software (Beckman Coulter).

462 *HeLa cells (Figure 2).* Cell death was assessed by propidium iodide (0.33 μg/ml)
463 nuclear staining recording over time using the IncuCyte live-cell imaging system
464 (Sartorius).
465 *HeLa cells (Figure 4)*. Five million cells were transiently transfected in two 10 cm dishes
466 (#CLS430591, Costar) with 2 μg hLyn[1-11]-hMTOR[2021-2113]-HA-mRFP-T2A-
467 hFKBP1A-Inp54p plasmid using the calcium-phosphate procedure. 24 h after
468 transfection, cells were washed with 5 ml of PBS and incubated with 1 ml of
469 trypsin/plate 10 min at 37°C, collected with 1 ml RPMI containing 10% FBS, centrifuged
470 for 3 min at 192 g at room temperature. Pellets were resuspended, seeded at a 300'000
471 cell density in 6 well plates (Costar, 3516) and cultured overnight in 10% FBS-
472 containing RPMI medium. They were then subjected to the indicated treatments. The
473 media was collected and kept aside, the cells were then washed with 1 ml of PBS,
474 incubated with 300 μl of trypsin for 10 min at 37°C, collected with the media kept aside
475 and centrifuged for 3 min at 192 g at 4°C. Pelleted cells were resuspended in 500 μl of
476 DAPI (1μg/ml) in PBS. The samples were analyzed by flow cytometry (Cytoflex S,
477 Beckman Coulter). DAPI incorporation was assessed in the RFP-positive cell fraction.
478 Data analysis was done with the Cytexpert software (Beckman Coulter).
479 *HeLa cells (Figure 5 and figure S1)* One hundred thousand cells were seeded in 12
480 well plates (Costar, 3513) in 10% FBS-containing RPMI medium and 14-18 h later and
481 treated as in the figures. The media was collected and kept aside, the cells were then
482 washed with 1 ml of PBS, incubated with 200 μl of trypsin for 10 min at 37°C, collected
483 with the media kept aside and centrifuged for 3 min at 192 g at 4°C. The cells were
484 then resuspended in 100 μl of PBS containing 8 μg/ml of propidium iodide and
485 incubated 5 min on ice in the dark. After transferring the samples to cytometer tubes
486 containing 300 μL of PBS, they were analyzed by flow cytometry with FC-500 Beckman

Coulter apparatus (Figure S1) or Cytoflex S Beckman Coulter apparatus (Figure 5). Data analysis was done with the Kaluza Version 1.3 software (Beckman Coulter) or the Cytexpert software (Beckman Coulter).

Mitochondria depletion

Mitochondria depletion was triggered by stimulating mitophagy like in [22]. Briefly, HeLa cells stably expressing a yellow fluorescent protein (YFP)-tagged Parkin construct were incubated 36 h with mitochondria damaging agents (1 μM antimycin A [cytochrome *c* reductase inhibitor]) and 1 μM oligomycin [ATP synthase inhibitor] or vehicle [ethanol 0.2%]. Mitochondria depletion blocks cell growth. Therefore, to ensure similar number of antimycin A- and oligomycin-treated cells versus control cells in 24 well plates (#CLS3527, Corning) after 36 h of culture, the initial seeding was 35'000 cells for the control condition and 150'000 cells for the antimycin A and oligomycin treatment. Mitochondria depletion was tested by immunoblotting against complex IV and cytochrome *C* or by staining the mitochondrial network with MitoTracker Red CMXRos (#M7512, ThermoFisher) according to manufacturer's instructions.

Composition of lipid mixtures

All lipids were purchased from Avanti Polar Lipids, except when indicated (Table 1). Lipids were dissolved to the desired concentration in chloroform and stored in glass tubes. Phosphoinositides phosphates and monosialgangliosides were dissolved in chloroform/methanol/H_2O 20:9:1. Lipid mixtures were assembled at the indicated ratios (mol %). Table 2 list reference plasma membrane composition used in this article.

Multilamellar vesicles (MLVs) generation and peptide binding

Given lipid mixtures indicated dried from organic solvents using an argon gas flux while vortexing to get a lipid film on the glass tube walls. The tubes were further dried vacuum-dried in a vacuum drying oven (SalvisLab) for 45 min at 50 ºC. PBS was added into lipid containing tubes to a final lipid concentration of 5 mg/ml. To favor solubility and formation of MLVs, the tubes were incubated 30 min at 37 ºC and finally vortexed. Homogeneous MLVs were generated after transfering the supsensions to Eppendorf tubes and performing three freeze/thaw cycles between liquid nitrogen and water bath set at 37 ºC. To assess peptide binding, MLVs were diluted at a 1 mg/ml concentration in a final volume of 50 µl PBS and incubated for 30 min at room temperature with 2 µM of the indicated FITC-labelled peptides. The lipophilic and hydrophilic fractions were separated by centrifugation at 21'000 g for 15 min. The hydrophilic fraction (~50 µl) was transferred to a 96 well black microtiter plates containing 50 µl of 0.2% Triton X-100 in PBS. The lipophilic fraction (the visible pellet) was resuspended in 50 µl of PBS and transferred to 96 well black microtiter plates containing 50 µl of 0.2% Triton X-100 in PBS. Fluorescence in each fraction was measured in a plate reader (Spectra MAX paradigm, Molecular devices) using emission/excitation at 480/560 nm. The percentage of binding was calculated by dividing the fluorescence found in the lipophilic fraction by the total fluorescence (lipophilic fraction + hydrophilic fraction).

Giant unilamellar vesicle (GUV) formation

GUVs were prepared by electroformation on indium tin oxide (ITO)-coated glass slides as described earlier [24]. Briefly, lipid mixes were diluted to a 1.5 mg/ml concentration in 140 µl of chloroform. The membrane of GUVs was stained through the addition of 1 µg of Texas Red 1,2-dihexadecanoyl-*sn*-glycero-3-phosphoethanolamine

triethylammonium salt (Texas Red DHPE). Then, 25 µl of the lipid mixture were spread in circles on ITO glass slides. Lipid mixtures were then vaccum-dryed in a vacuum drying oven at 50 ºC for 30 min. Electroformation chambers were created using a spacer between two ITO glasses and around the dried lipid deposit. Electroformation chambers were filled with 400 µl of water solution containing 300 mM saccharose. The ITO glasses were connected to AC generator (#459AL, Kikusui Electronics) with a sinusoidal current (1 mV, 10 Hz) for 1 hour. Then, GUVs were collected into Eppendorf tubes and used immediately for permeabilization experiments.

GUV permeabilization experiments

Glass bottom 96 well plate (#PBK96G-1.5-5-F, MatTek Corporarion) were blocked at room temperature with 10 mg/ml BSA (bovine serum albumin) in PBS for at least 30 min. The wells were then washed 5 times with distilled water and filled with 100 µl of PBS containing 5 µM calcein and the figure-indicated peptide concentrations. GUVs (10 µl), prepared as described in the previous section, were then added to each well. After 60 min of incubation at room temperature, images were taken (at least 5 per condition) using confocal microscopy. The percentage of GUV permeabilization was assessed by measuring the extent of calcein fluorescence inside the GUVs versus outside. Image analysis was performed using the software developed in [25]. The experiments were repeated twice and at least 150 vesicles per condition were included.

Atomic force microscopy

559 Lipid unilamellar vesicles containing (mol %) PC 51.25%, PE 36.25, PS 10%, PI(4.5)P_2
560 2.5% which were fused on mica with PBS supplemented with 10 mM $CaCl_2$ at 70 °C
561 for 45 min to form supported lipid bilayer (SLB). After 9 min cooling down, the SLBs
562 were washed with imaging buffer (Tris-HCl 50 mM pH 7.4, KCl 300 mM) containing 10
563 mM EDTA to remove calcium. Lipid bilayers were incubated for 30 min with 10 µM of
564 TAT-RasGAP$_{317-326}$ or W317A peptide dissolved in the imaging buffer. AFM imaging
565 was performed using a multimode AFM instrument equipped with Nanoscope VIII
566 (Bruker Nano Surfaces). All AFM images were acquired in Peak Force Taping mode
567 at room temperature under liquid conditions (imaging buffer solution) using V-shaped
568 silicon nitride cantilevers (MLCT probe from Bruker Nano Surfaces or OMCL-
569 TR800PSA from Olympus).

570

571 **PI(4,5)P_2 depletion**

572 PI(4,5)P_2 plasma membrane depletion assay was performed using a rapamycin-
573 triggered plasma membrane recruitment of a lipid phosphatase removing the
574 phosphate at position 5 on the inositol ring of PI(4,5)P_2 [26] (see Figure 4A-B for
575 details). Three hundred thousand HeLa cells were seeded in 35 mm glass bottom
576 dishes (#P35G-1.5-4-C, MatTek) and transfected by calcium phosphate for 16 h with
577 the hLyn[1-11]-hMTOR[2021-2113]-HA-mRFP-T2A-hFKBP1A-Inp54p plasmid (1.5
578 µg) and the PH-PLCD1[1-170]-GFP plasmid (0.5 µg). After 10 h of recovery in RPMI
579 10% FBS the transfected cells were treated 1 h with rapamycin (400 nM) or vehicle
580 (0.2% DMSO) before imaging. When PI(4,5)P_2 plasma membrane is depleted, the
581 GFP-PH sensor translocates to the cytoplasm. Cytosolic GFP was quantitated by
582 manually selecting regions of interest (ROI) in the cytosol and measuring the pixel
583 intensity median using the ROI Manager tool of the FIJI software [27]

584

585 **Immunoblotting**

586 For the detection of cytochrome *c*, cytochrome *c* oxidase and HA tag, cells were lysed
587 in NP-40 lysis buffer (NaCl 150 mM, NP-40 1%, TrisHCl 50 mM pH 8, protease and
588 phosphorylation inhibitors). Primary and secondary antibodies were used at a 1:1000
589 and a 1:5000 dilution, respectively. Visualization of the bands was performed using the
590 ChemiDoc apparatus (Bio-Rad) for HRP conjugate antibodies and Odyssey LI-COR
591 scanner apparatus (LI-COR Biosciences) for Alexa Fluor 680 conjugated antibodies.

592

593 **Deep-etched electron microscopy**

594 Fifty thousand HeLa cells were seeded in RPMI 10% FBS media the day prior
595 treatments in 24 well plates (Costar, 3526) containing two small coverslips. After the
596 indicated treatments, the cells were washed two times with PBS and fixed in a 2%
597 glutaraldehyde solution (100 mM NaCl, 30 mM HEPES [pH7.2], 2 mM $MgCl_2$, 150 mM
598 sucrose) for 30 min at room temperature. Platinum replicas were prepared as
599 described previously [28], examined with a 100CX microscope (JEOL JEM 1400,
600 Peabody, MA) and imaged with an AMT digital camera (Danvers, MA).

601

602 **Confocal microscopy**

603 GUV calcein intake and $PI(4,5)P_2$ depletion imaging were done with an LSM710
604 confocal microscope equipped with a Plan-Apochromat 63X/1.40 Oil Immersion (for
605 GUVs) and Plan-Neofluar 40x/1.30 Oil DIC M27 (for cells) objectives (Zeiss,
606 Oberkochen, Germany) respectively. Excitation light came from an Argon ion laser
607 (488 nm) and a diode-pumped solid-state laser (561 nm). A spectral beam guide was

used to separate emitted fluorescence. Live cell imaging was done in an incubation chamber set at 37 °C and 5% CO_2.

Epifluorescence imaging

MitoTracker staining imaging was performed with an Axiovert 40 inverted microscope equipped with epifluorescence utilities, using the AxioVision microscopy software (Zeiss Oberkochen, Germany). The excitation light came from a mercury lamp (578 nm).

In silico modelling

The interactions of TAT-RasGAP$_{317-326}$ (DTRLNTVWMWGGRRRQRRKKRG) and W317A mutant (DTRLNTVWMAGGRRRQRRKKRG) peptides in D amino acids and inverso configuration with different type of lipid bilayers was investigated through molecular dynamics (MD) simulations. TAT-RasGAP$_{317-326}$ and W317A peptides were obtained following a procedure used of recent work [29]. Both peptides were inserted at a minimum distance of 2 nm from the different symmetric multi-component bilayers, constructed and solvated with TIP3P [30] water model using CHARMM-GUI [31-33]. The composition of each layer of the different type of membrane is described in Table 3. Both peptides were simulated in 4 replicas for all the different membrane composition, generating a total number of 48 systems. The systems were composed of 38000 total particles, after addition of sodium and chloride ions at a concentration of 0.15M. The “inner leaflet” system was the only one composed by 48000 total particles. The CHARMM36 [34, 35] force field was used to define phospholipids and proteins topology through an all-atom approach. Each system was minimized using

the steepest descent method and then, was performed an equilibration procedure through one MD simulation of 50 ps under NVT ensemble and four MD simulations of 50 ps, 100 ps, 100 ps, and 200 ps under the NPT ensemble. Phospholipids position restraints were applied during the first four MD simulations and gradually removed, from 1000 kJ/mol*nm2 to 40 kJ/mol*nm2. Instead peptides position restraints ware maintained for all the equilibration process at 1000 kJ/mol*nm2. For the equilibration protocol, the velocity rescaling [36] temperature coupling algorithm with a time constant of 1.0 ps were applied to keep the temperature at 310.00 K. Berendsen [37] semi-isotropic pressure coupling algorithm with reference pressure equal to 1 bar and time constant 5.0 ps was employed. Then, all systems were simulated for the production run in the NPT ensemble with the time step of 2 fs, using Nose-Hoover1 [38] thermostat and Parrinello-Rahman [37] barostat. The overall sampled time for all systems were 200 ns, except for the inner leaflet system, which was simulated for 500 ns. Electrostatic interactions were calculated by applying the particle-mesh Ewald [39] (PME) method and van der Waals [40] interactions were defined within a cut-off of 1.2 nm. Periodic boundary conditions were applied in all directions. Trajectories were collected every 2 ps and the Visual Molecular Dynamics [41] (VMD) package was employed to visually inspect the simulated systems. GROMACS 2018 [42, 43] package was used for simulations and data analysis. The last 20 ns of the 200 ns production run of each simulation was taken into account for all the analyses. In addition, the last 50 ns of 500 ns or the whole production run of INNER-system was considered for further analyses.

Circular dichroism (CD) sample preparation

UV-controlled stock solutions of peptides were prepared in water-acetonitrile (2:1 vol.) mixtures and aliquots of ca. 50 µmol were freeze-dried before measurements. The isotropic samples (PB (phosphate buffer, 10 mM, pH 7.4), PB:TFE, TFE, ultrapure deionized water (Milli-Q, Merck-Millipore) were freshly assembled by directly adding the solvents at room temperature. The solutions (suspensions) were rigorously vortexed/bath-sonified until clear and immediately transferred to the measurement cuvettes. The samples with the addition of detergent micelles or phospholipid SUVs were done by an equivolume mixing of the peptide PB solutions with the separately prepared membrane mimetics, followed by gentle (by hand) mixing. Detergent micelles were prepared in PB by dissolving appropriate amounts of detergents, followed by vigorous vortexing, room temperature bath-sonification, brief centrifugation – to deplete the foam formation. SUVs for addition to peptides were formed by first co-dissolving desired lipid mixtures in methanol/chloroform (1:9), followed by the solvent removal (N_2-flow and vacuum overnight). Obtained lipid cakes were suspended in PB with vortexing, 10x freeze/thaw cycles (N_2-Liq/ water bath equilibrated at a temperature above the main lipid melting transition of the lipid with the highest value thereof) to prepare the MLVs. SUVs were generated by sonication of the suspension for 16 min in a strong ultrasonic device (UTR 200, Hielscher, Germany). A constant sample temperature above the mixture melting point was maintained by circulating water from a thermostat connected to the sonicator, thus preventing overheating of the sample during sonication. The same procedure was employed when proteoliposomes were formed, only that the peptides were added to the initial methanol/chloroform solutions. After measurements, the samples were subjected to UV-absorbance re-evaluation to control the factual peptide concentrations.

CD spectroscopy

Circular dichroism spectra were recorded a Jasco J-815 CD spectropolarimeter using a home-built nitrogen flow regulator. Rectangular quartz cuvettes (Suprasil®) of 1 mm path length from Hellma were used. All spectra were measured at a controlled temperature (37°C or above the lipid melting point) using the standard Jasco setup of a sample holder connected to an external water thermostat (Julabo). The spectra were recorded from 260 to 185 nm. The measurements were performed in the continuous scanning mode using 1 nm spectral bandwidth, 0.1 nm data pitch, and 8 s response time of the detector. Three consecutive scans were collected at a rate of 20 nm/min and averaged for each spectrum, including the backgrounds. The background spectra were subtracted from the sample spectra after the measurements; results were corrected to zero ellipticity at 260 nm, and individually scaled (according to tryptophan absorbance readout of the withdrawn samples). Spectral acquisition and all processing steps were performed using the preinstalled software package of the spectropolarimeter (Jasco).

Solid-state nuclear magnetic resonance (ssNMR) sample preparation

Macroscopically oriented membrane samples for solid-state ^{31}P-NMR measurements were prepared by hydrating peptide/lipid multibilayers on glass supports, as described previously [15]. Peptides were used at 1:100 peptide/lipid ratio, and lipid membranes were either pure DOPE or DOPE/DOPG (100/1) or DOPE/DOPS (100/1). The peptides were dissolved in methanol, the lipid in methanol:chloroform (1:9), to provide initial stock solutions. Appropriate aliquots of peptide and lipid were combined in excess 1:1 chloroform:methanol solution. Resulting mixtures were deposited on ten ultrathin (12×7.5×0.08 mm) glass slides (Paul Marienfeld). A total 3.2-3.5 mg of lipid was used

for each sample. Typically, per glass slide, ca. 30 µl of the solution containing ca. 0.3 mg total material was spread and dried under vacuum for 6 h. Glass slides were supplemented each with 1 µl ultrapure deionized water (milli-Q), manually assembled in stacks, and equilibrated for 16-24 h in a sealed plastic container in the presence of water (at 4 °C, below the DOPE phase transition temperature). The stacks were wrapped on ice in several layers of a stretched parafilm and a polyethylene foil, to maintain hydration during the experiments. Samples were kept on ice before the measurements.

^{31}P ssNMR spectroscopy

Solid-state ^{31}P-NMR experiments were performed on a wide bore AVANCE III spectrometer (Bruker), operating for ^{31}P at 202.46 MHz. The spectra were recorded using a Bruker static triple-resonance (HX(Y)) probe, equipped with a home-built proton RF-coil with a low inductance (low-E coil), to avoid heating, employing a standard Hahn-echo pulse sequence and a two-pulse phase-modulated proton decoupling (Bruker TPPM-20 decoupling sequence, 30 kHz). The X-channel 90° pulse length of 4 µs, echo-delay time of 30 µs, 100 kHz spectral width, and a recycle time of 2 s were applied. Standard temperature regulating equipment of the spectrometer was used, which was automatically controlling the sample temperature by heating an externally cooled airflow (1000 L/h). The explored temperature ranged nominally between 278-323 K and was using 5 K temperature steps in the heating mode. For each spectrum, 128 scans were obtained, using a 60 s pre-acquisition delay for the temperature equilibration. Extra care was taken to assure that each sample experienced an identical thermal history. Spectrum processing was performed by using Bruker TopSpin 4.0.6 software.

Acknowledgements

We would like to thank Navin Gopaldass and Andreas Mayer for liposomes technical support and Dora Hancz and Petr Broz for providing the HeLa dominant negative CHMP3$^{1-179}$ and VPS4A^{E228Q} cell lines. We acknowledge the support from France-BioImaging (FBI, ANR-10-INSB-04). This work was supported by a grant from the Swiss National Supercomputing Centre (CSCS).

Tables

Table 1 Lipids used in this study

This table lists the lipids used for performing of MLVs binding, GUVs permeabilization, AFM, CD, and ^{31}PssNMR experiments. Unless otherwise indicated, the lipids were purchased from Avanti Polar Lipids.

MLVs & GUVs	
LIPID	**REFERENCE #**
Phosphatidylcholine (PC) (Egg)	840051
Phosphatidylethanolamine (PE) (Egg)	840021
Sphingomyelin (SM) (Egg)	860061
Phosphatidylserine (PS) (Brain)	840032
Phosphatidic acid (PA) (16:0-18:1)	840857
Phosphatidylinositol (PI) (Liver)	840042
Cholesterol (CHL) (Ovine)	700000
Monosialotetrahexosylganglioside (GM1) (Ovine brain)	860065
Monosialodihexosylganglioside (GM3) (Bovine milk)	860058
Phosphatidylinositol(4.5)phosphate (PI(4.5)P2) (18:1)	850155
Phosphatidylinositol(3.5)phosphate (PI(3.5)P2) (18:1)	850154
Phosphatidylinositol(3)phosphate (PI(3)P) (18:1)	850150
Phosphatidylinositol(3.4)phosphate (PI(3.4)P2) (18:1)	850153
Phosphatidylinositol(3.4.5)phosphate (PI(3.4.5)P2) (18:1)	850156
Cardiolipin (CAR) (18:1)	710335
Texas Red DHPE	T1395MP (ThermoFisher)
AFM	
LIPID	**REFERENCE #**
Phosphatidylcholine (PC) (Egg)	840051
Phosphatidylethanolamine (PE) (16:0-18:1)	850757
Phosphatidylserine (PS) (16:0-18:1)	840034
Phosphatidylinositol(4.5)phosphate (PI(4,5)P2) (18:0-20:4)	850165
CD	
LIPID	**REFERENCE #**
Dodecylphosphocholine (DPC)	850336P (Sigma-Aldrich)
Lyso-phosphatidylglycerol (oPG) (18:1)	858125
Lyso-phospatidylcholine (mPC) (14:0)	855575
Sodium dodecyl sulfate (SDS)	CP29.2 (Carl Roth)
^{31}P-ssNMR	
LIPID	**REFERENCE #**

Pphosphoethanolamine (PE, DOPE) (18:1)	850725
Phosphatidylglycerol (PG, DOPG) (18:1)	840475
Phosphatidylserine (PS, DOPS) (18:1)	840035

745

746

747 **Table 2 Plasma membrane composition**

748 This table lists the lipid composition of the inner and outer leaflets of the plasma
749 membrane (mol %) (from [44]) that was used in the present work.

Lipids	Inner leaflet (%)	Outer leaflet (%)
Phosphatidylcholine (PC)	17.3	35.7
Phosphatidylethanolamine (PE)	25.4	5.6
Sphingomyelin (SM)	9.3	19.2
Phosphatidylserine (PS)	10.7	0
Monosialotetrahexosylganglioside (GM1)	0	2.6
Monosialodihexosylganglioside (GM3)	0	2.6
Phosphatidylinositol (PI)	4.6	0
Phosphatidic acid (PA)	1.5	0
Phosphatidylinositol (4,5) biphosphate [$PI(4,5)P_2$]	1.5	0
Lysophosphatidylcholine (LPC)	0	1.3
Cholesterol (CHL)	28.5	31.3

750

751

Table 3 Membrane compositions used in the *in silico* simulations

Membranes composition used for *"in silico"* simulations Total number of lipid molecules used per layer are indicated.

	POPC	SLPE	PSM	CHL	SOPS	POPA	SAPI	TOCAR	POPI(4,5)P2	Total
PC (100%)	55	-	-	-	-	-	-	-	-	55
PS (20%)	44	-	-	-	11	-	-	-	-	55
PA (20%)	44	-	-	-	-	11	-	-	-	55
PI(4,5)P2 (5%)	52	-	-	-	-	-	-	-	3	55
CAR (10%)	49	-	-	-	-	-	-	6	-	-
Inner leaflet	14	20	8	23	9	1	4	-	1	80

CHL, cholesterol; POPA (16:0-18:1 PA); POPC (16:0-18:1 PC); SLPE (18:0-18:2 PE); SAPI (18:0-20:4 PI); POPI(4,5)P_2 (16:0-18:1), POPI(4,5)P_2 (16:0-18:1 PI(4,5)P_2); SOPS (18:0–18:1 PS); PSM (16:0 SM); TOCAR (18:1 CAR).

Figure legends

Figure 1 Preferential binding of TAT-RasGAP$_{317-326}$ to inner leaflet phospholipids

Multilamellar vesicles (MLVs) were generated with the indicated percentages of the specified lipids at the figure (the remaining lipid being phosphatidylcholine). Outer leaflet liposomes contained PC 64.4%, PE 10.6%, SM 20%, GM1 2.5%, GM3 2.5% while inner leaflet liposomes contained PC 51.25%, PE 36.25%, PS 10%, PI(4.5)P_2 2.5%. Liposomes were incubated 30 min with 2 µM of FITC-labelled versions of TAT, TAT-RasGAP$_{317-326}$, and TAT-RasGAP$_{317-326}$(W317A). Binding of these peptides to liposomes was then determined (n=4). The zones highlighted in light grey correspond to the physiological concentrations found in plasma membranes. Statistical analysis was performed using one-way ANOVA with Geisser-Greenhouse correction (sphericity not assumed), followed by post-hoc Tuckey multi-comparison tests between means of all groups.

Figure 2 TAT-RasGAP$_{317-326}$ kills HeLa cells in a mitochondria-independent manner

A. GUVs containing 10% cardiolipin were incubated or not for 1 h with TAT-RasGAP$_{317-326}$ or TAT-RasGAP$_{317-326}$(W317A) at the indicated concentrations. GUVs permeabilization was evaluated by calcein intake using confocal microscopy. Representative images are presented (scale bar: 10 µm) and quantitation is shown as violin plots (dark grey bars indicate the median). **B**-**C**. HeLa cells ectopically expressing YFP-Parkin were incubated 36 h with 1 µM antimycin A and 1 µM oligomycin (A/O) or vehicle (ethanol 0.2%) (Control). Mitochondria were then stained with the MitoTracker

dye (scale bar: 20 µm) (panel B). Alternatively, the expression of cytochrome *c* (Cyt *c*), cytochrome *c* oxidase (COX IV) and actin in these cells was assessed by western blot analysis (panel C). **D**. HeLa cells ectopically expressing YFP-Parkin were treated as in panel B-C. They were then incubated with the indicated compounds for various periods of time (ActD, actinomycin D; ABT, ABT737). Cell death was assessed using a live-cell imaging system (see material and methods). Results are expressed as the mean ± standard deviation of three biologically independent experiments.

Figure 3 TAT-RasGAP$_{317-326}$ permeabilizes membranes made of inner leaflet phospholipids

GUVs made of lipid mixtures mimicking the outer leaflet (PC 64.4%, PE 10.6%, SM 20%, GM1 2.5%, GM3 2.5%) or inner leaflet (PC 51.25%, PE 36.25%, PS 10%, PI(4.5)P_2 2.5%) plasma membrane composition and GUVs containing 2.5% PI(4,5)P_2 (and 97.5% PC) or 10% PS (and 90% PC) were treated or not for 1 hour with TAT-RasGAP$_{317-326}$ or TAT-RasGAP$_{317-326}$(W317A) at the indicated concentrations. GUV permeabilization was evaluated by calcein intake using confocal microscopy. Representative images are presented (scale bar: 10 µm) and quantitation is shown as violin plots (median is indicated by a dark grey bar). See Table 2 for lipid abbreviations.

Figure 4 PI(4.5)P_2 plasma membrane depletion impairs TAT-RasGAP$_{317-326}$-induced cell death

A. Schematic description of the plasmid (hLyn[1-11]-hMTOR[2021-2113]-HA-mRFP-T2A-hFKBP1A-Inp54p) encoding the protein constructs allowing rapamycin-controlled

809 $PI(4,5)P_2$ dephosphorylation. This plasmid contains an open reading frame encoding
810 two proteins separated by a self-cleaving T2A peptide [45], the sequence of which is
811 shown in blue with the cleavage site indicated by an arrowhead. The first protein
812 corresponds to a fusion protein between the monomeric red fluorescent protein
813 (mRFP) and the FKBP rapamycin binding (FRB) domain of human mammalian target
814 of rapamycin (mTOR). This fusion protein is tagged at the N-terminus with the first 11
815 amino acids of human Lyn that allows plasma membrane targeting via myristoylation
816 and palmitoylation [46]. An HA tag is located between FRB and mRFP (not shown in
817 the figure). The second protein is a fusion protein between Inp54p, a yeast
818 phosphatidylinositol-4,5-bisphosphate 5-phosphatase [47] and the human FK506
819 binding protein FKBP1A (also known as FKBP12). **B**. Scheme depicting the principle
820 of the procedure allowing $PI(4,5)P_2$ depletion at the plasma membrane level. In the
821 presence of rapamycin, FRB and FKBP12 dimerize resulting in plasma membrane
822 targeting of Inp54p. Panels A and B were adapted from [26]. **C**. HeLa cells were
823 transiently transfected (at 3:1 ratio) with the construct depicted in panel A and PH-
824 PLCD1[1-170]-GFP, a plasmid encoding a fusion protein between GFP and the
825 pleckstrin homology (PH) domain of PLCδ1. This PH domain binds to $PI(4,5)P_2$ and
826 functions as a $PI(4,5)P_2$ localization biosensor in cells. The transfected cells were
827 treated 1 hour with rapamycin (400 nM) or vehicle (0.2% DMSO) and then were
828 subjected to live imaging using confocal microscopy (scale bar: 20 μm). Cytosolic GFP
829 fluorescence was quantitated as indicated in the methods. Dots correspond to
830 individual cells. Medians are indicated by red bars. **D**. HeLa cells were transiently
831 transfected with the construct depicted in panel A. The cells were then pretreated 1
832 hour with 400 nM of rapamycin or vehicle (0.2% DMSO), followed by 6 hour incubation
833 with the indicated concentrations of TAT-$RasGAP_{317-326}$. Plasma membrane

permeabilization was tested by DAPI staining and measured by flow cytometry in mRFP-positive cells. **E**. Alternatively, following the rapamycin treatment, the cells were subjected to 1 hour incubation with 20 μM FITC-labelled TAT-RasGAP$_{317-326}$. Peptide uptake was evaluated in mRFP-positive cells by flow cytometry. FITC fluorescence was normalized against the "DMSO + peptide" condition. Statistical analysis was performed using paired t-test (panels C and E) or two-way ANOVAs followed by post-hoc Sidak's multi-comparison test with matched comparison (panel D). In panels D and E, each point represents an individual experiment and the horizontal black bars correspond to the median. Values from a given independent experiment are connected with thin black lines.

<u>Figure 5</u> Dominant negative mutants of the ESCRT machinery sensitize cells to TAT-RasGAP$_{317-326}$-induced death

A. HeLa cells expressing the doxycycline-inducible HA-tagged CHMP3$^{1-179}$ and VPS4A^{E228Q} constructs were treated with doxycycline for the indicated periods of time. Expression of the tagged proteins was assessed by Western blot. Vinculin and β-actin were used as loading controls (vinculin was used for VPS4A^{E228Q}-inducible cells as β-actin and VPS4A have similar apparent molecular weight). **B**. Control HeLa cells and the HeLa clones described in panel A were stimulated 6 h in the presence or in the absence of doxycycline and then incubated, still in the presence of doxycycline, with the indicated concentrations of TAT-RasGAP$_{317-326}$ for 6 additional h. Plasma membrane damage was tested by flow cytometry after PI staining. Values from a given independent experiment are connected with thin black lines. **C**. Alternatively after the doxycycline stimulation, cells were incubated with a sub-lethal concentration (10 μM)

of FITC-labelled TAT-RasGAP$_{317-326}$ for 1 hour. Peptide uptake was measured by flow cytometry. Fluorescence from the plasma membrane-attached peptide was quenched with 0.2% trypan blue. The data was normalized against the “non-induced + peptide” condition. Two-way ANOVAs followed by post-hoc Sidak’s multi-comparison test with matched comparison (panel B) and paired t-test (panel C) were used to assess the significance of the observed differences.

Figure 6 The W317A mutation promotes alpha helix formation in the RasGAP moiety of TAT-RasGAP$_{317-326}$

The secondary structure of TAT-RasGAP$_{317-326}$ in the presence of the indicated membrane lipid environment was assessed by *in silico* simulations as described in the methods (4 simulations per condition). The membrane compositions are presented in Table 3. The graph depicts the α helicity content in the whole TAT-RasGAP$_{317-326}$ peptide as well as in its individual TAT and RasGAP$_{317-326}$ moieties. The median is indicated by black bars. Paired t-tests were used to assess statistical significance. The structures presented below the graphs are snapshot examples of the structures obtained for TAT-RasGAP$_{317-326}$ and its W317A mutant in inner leaflet-like membrane system.

Figure 7 The W317A mutation affects the structure of TAT-RasGAP$_{317-326}$ and its ability to interact with membranes

A. The propensity of TAT-RasGAP$_{317-326}$ and its W317A mutant to penetrate membranes with the indicated compositions (see Table 3) was analyzed by computing

881 the buried surface with GROMACS tools and homemade scripts. The graph on the left
882 presents the surface of the peptides buried within all the lipids of the contacting leaflet,
883 while the graph on the right only considers the surface of the peptides buried within
884 neutral lipids of the membrane (e.g. PC). Paired t-tests were used to assess statistical
885 significance. The images below the graphs are snapshots of the interaction of TAT-
886 RasGAP$_{317-326}$ and its W317A mutant in inner leaflet like-membranes. The peptides
887 stay superficially bound and are located within the light gray ovals. **B**. Probability of the
888 individual residues within TAT-RasGAP$_{317-326}$ or its W317A mutant to establish contact
889 with inner leaflet composition membrane. The results correspond to the median of four
890 separate simulations. **C**. In the image shown on the left, θ corresponds to the angle
891 between the membrane normal (Z) and the long axis of the helically folded TAT
892 segment (Cα (Arg)-Cα(Gly) vector). The graph shows the median change of this angle
893 in 4 separated simulations of TAT-RasGAP$_{317-326}$ and its W317A mutant in inner leaflet-
894 like membranes. The images below depict simulation snapshots of peptide interaction
895 with inner leaflet composition membrane (see Table 3). Only the peptides and
896 cholesterol molecules are shown and thin lines represent the limit of phospholipid
897 heads.

898

899 **<u>Figure 8</u> TAT-RasGAP$_{317-326}$ mode of action**

900 TAT-RasGAP$_{317-326}$-induced cell death current model: TAT-RasGAP$_{317-326}$ crosses the
901 plasma membrane thanks to the formation of transient water pores[17]. Once inside
902 the cytosol, TAT-RasGAP$_{317-326}$ interacts with phospholipids (PIP_2 and PS) enriched in
903 the inner layer of the plasma membrane. This triggers membrane disruption in a
904 detergent-like manner, eventually leading to cell lysis.

Supplementary Figure legends

Figure S1 TAT-RasGAP$_{317-326}$ does not form streptolysin O-like pores

A-**D**. HeLa cells were left untreated (panel A), incubated with streptolysin O (SLO) (50-100 units/ml) for 5 min (panel B), or treated with 60 μM TAT-RasGAP$_{317-326}$ for 2 h (panels C and D) in RPMI, 10% FBS at 37°C. Cells were then analyzed by deep-etched electron microscopy. The insets in panel B show SLO-induced pores at high magnification. Panel C depicts a cell membrane that has not suffered marked perturbations from TAT-RasGAP$_{317-326}$ while panel D shows a membrane disrupted by the peptide. Scale bars: 500 nm (100 nm in the insets). **E**. HeLa cells were treated with 60 μM TAT-RasGAP$_{317-326}$ for the indicated periods of time. Cell integrity was assessed by flow cytometry after PI staining.

Figure S2 The TAT-RasGAP$_{317-326}$ (W317A) point mutant has impaired killing abilities

Raji cells were incubated 1 h (panels **A**, **B**, and **D**) or 24 h (panel **C**) with the indicated concentrations of FITC-labelled wild-type and W317A version of TAT-RasGAP$_{317-326}$. Cell death and peptide uptake were determined by flow cytometry as described in the methods. Fluorescence from the plasma membrane-attached peptide was quenched with 0.2% trypan blue. Medians are indicated by dark grey bars.

Figure S3 TAT-RasGAP$_{317-326}$ does not efficiently permeabilize cardiolipin-containing vesicles

GUVs containing 20% CAR (and 80% PC) were treated or not for 1 h with TAT-RasGAP$_{317-326}$ or TAT-RasGAP$_{317-326}$(W317A) at the indicated concentrations. GUVs permeabilization was evaluated by calcein intake using confocal microscopy. Representative images are presented (scale bar: 10 µm) and quantitation is shown as violin plots (medians are indicated by dark grey bars).

Figure S4 Effect of TAT-RasGAP$_{317-326}$ on phosphatidylcholine-containing GUVs

GUVs made only of PC were treated or not for 1 h with TAT-RasGAP$_{317-326}$ or TAT-RasGAP$_{317-326}$(W317A) at the indicated concentrations. GUVs permeabilization was evaluated by calcein intake using confocal microscopy. Representative images are presented (scale bar: 10 µm) and quantitation is shown as violin plots (medians are indicated by dark grey bars).

Figure S5 TAT-RasGAP$_{317-326}$ permeabilizes PI(3,4)P$_2$- and PI(3,5)P$_2$-containing GUVs

GUVs containing 2.5% PI(3.4)P$_2$ or 2.5% PI(3,5)P2 (and 97.5% PC) were treated or not for 1 h with TAT-RasGAP$_{317-326}$ or TAT-RasGAP$_{317-326}$(W317A) at the indicated concentrations. GUVs permeabilization was evaluated by calcein intake using confocal microscopy. Representative images are presented (scale bar: 10 µm) and quantitation is shown as violin plots (medians are indicated by dark grey bars).

Figure S6 TAT-RasGAP$_{317-326}$ permeabilizes in a detergent-like manner membranes made of phospholipids present in the inner layer of the plasma membrane

Supported lipid bilayers (SLBs) mimicking the inner leaflet of the plasma membrane [PC 51.25%, PE 36.25%, PS 10%, PI($_{4.5}$)P$_2$ 2.5%] were treated with 10 µM of TAT-RasGAP$_{317-326}$ or TAT-RasGAP$_{317-326}$(W317A) peptide for 30 min. Images were taken by AFM at a z scale of 10 nm. Representative images are presented (scale bars: 500 nm).

Figure S7 Wild-type and mutant (W317A) TAT-RasGAP$_{317-326}$ secondary structure in aqueous and membrane mimicking environments

A. Spectral line shapes for an ideal α-helix, ideal β-strand and 100% random coil of an arbitrary D-amino acid composed peptide. Purple and red arrows point to the characteristic π→π* and n→π* transitions, respectively. **B**. Experimental far-UV circular dichroism spectra of TAT-RasGAP$_{317-326}$ and W317A measured at 37°C in different environments: H_2O, PB (phosphate buffer, 10 mM, pH 7.4), PB:TFE 50:50, pure TFE, DPC, mPC, SDS and oPG.

Figure S8 Membrane curvature-modulating properties of wild-type and mutant (W317A) TAT-RasGAP$_{317-326}$

A. Scheme illustrating the lamellar to hexagonal transition and the positive and negative curvatures in a lipid bilayer. **B.** Temperature-dependent ^{31}P ssNMR spectral series from macroscopically aligned DOPE membranes (left panel), DOPE:DOPG

(middle panel) and DOPE:DOPS (right panel) treated or not with the indicated peptides. Resonance frequencies assigned to the lamellar (L) and inverted hexagonal (H_{II}) are marked in the DOPE control. Red dots depict approximate centers of the L-to-H_{II} phase transition, corresponding to approximately 50% L 50% H_{II} state (i.e., T_{L-H}).

Reference list

1. Valentin, R., S. Grabow, and M.S. Davids, *The rise of apoptosis: targeting apoptosis in hematologic malignancies.* Blood, 2018. **132**(12): p. 1248-64.
2. Fernald, K. and M. Kurokawa, *Evading apoptosis in cancer.* Trends Cell Biol, 2013. **23**(12): p. 620-33.
3. Hanahan, D. and R.A. Weinberg, *Hallmarks of cancer: the next generation.* Cell, 2011. **144**(5): p. 646-74.
4. Michod, D., et al., *A RasGAP-derived cell permeable peptide potently enhances genotoxin-induced cytotoxicity in tumor cells.* Oncogene, 2004. **23**(55): p. 8971-8.
5. Barras, D., et al., *Inhibition of cell migration and invasion mediated by the TAT-RasGAP317-326 peptide requires the DLC1 tumor suppressor.* Oncogene, 2014. **33**(44): p. 5163-72.
6. Chevalier, N., N. Gross, and C. Widmann, *Assessment of the chemosensitizing activity of TAT-RasGAP317-326 in childhood cancers.* PLoS One, 2015. **10**(3): p. e0120487.
7. Tsoutsou, P., et al., *TAT-RasGAP317-326 enhances radiosensitivity of human carcinoma cell lines in vitro and in vVivo through promotion of delayed mitotic cell death.* Radiat Res, 2017. **187**(5): p. 562-569.
8. Michod, D., et al., *Effect of RasGAP N2 fragment-derived peptide on tumor growth in mice.* J Natl Cancer Inst, 2009. **101**(11): p. 828-32.
9. Heulot, M., et al., *The anticancer peptide TAT-RasGAP317-326 exerts broad antimicrobial activity.* Front Microbiol, 2017. **8**: p. 994.
10. Heulot, M., et al., *The TAT-RasGAP 317-326 anti-cancer peptide can kill in a caspase-, apoptosis-, and necroptosis-independent manner.* Oncotarget, 2016. **7** (39): 64342-59.
11. Barras, D., et al., *A WXW motif is required for the anticancer activity of the TAT-RasGAP317-326 peptide.* J Biol Chem, 2014. **289**(34): p. 23701-11.
12. Jimenez, A.J., et al., *ESCRT machinery is required for plasma membrane repair.* Science, 2014. **343**(6174): p. 1247136.
13. Rühl, S., et al., *ESCRT-dependent membrane repair negatively regulates pyroptosis downstream of GSDMD activation.* Science, 2018. **362**(6417): p. 956-960.
14. Reid, L.M., C.S. Verma, and J.W. Essex, *The role of molecular simulations in understanding the mechanisms of cell-penetrating peptides.* Drug Discovery Today, 2019. **24**(9): p. 1821-1835.
15. Murayama, T., et al., *Loosening of lipid packing promotes oligoarginine entry into cells.* Angewandte Chemie International Edition, 2017. **56**(26): p. 7644-7647.
16. Afonin, S., et al., *The cell-penetrating peptide TAT(48-60) induces a non-lamellar phase in DMPC membranes.* Chemphyschem, 2006. **7**(10): p. 2134-42.
17. Trofimenko, E., et al., *Potassium channels, megapolarization, and water pore formation are key determinants for cationic cell-penetrating peptide translocation into cells.* bioRxiv, 2020: p. 2020.02.25.963017.
18. Paterson, D.J., et al., *Lipid topology and electrostatic interactions underpin lytic activity of linear cationic antimicrobial peptides in membranes.* Proc Natl Acad Sci USA, 2017. **114**(40): p. E8324-E8332.
19. Deslouches, B. and Y.P. Di, *Antimicrobial peptides with selective antitumor mechanisms: prospect for anticancer applications.* Oncotarget, 2017. **8**(28): p. 46635-51.
20. Raucher, D. and J.S. Ryu, *Cell-penetrating peptides: strategies for anticancer treatment.* Trends Mol Med, 2015. **21**(9): p. 560-570.
21. Baxter, A.A., I.K. Poon, and M.D. Hulett, *The plant defensin NaD1 induces tumor cell death via a non-apoptotic, membranolytic process.* Cell Death Discov, 2017. **3**: p. 16102.
22. Correia-Melo, C., et al., *Depletion of mitochondria in mammalian cells through enforced mitophagy.* Nat Protoc, 2016. **12**(1): p. 183-94.

23. Jordan, M., A. Schallhorn, and F.M. Wurm, *Transfecting mammalian cells: optimization of critical parameters affecting calcium-phosphate precipitate formation.* Nucleic Acids Res, 1996. **24**(4): p. 596-601.
24. Angelova, M.I., et al. *AC Field Controlled Formation of Giant Fluctuating Vesicles and Bending Elasticity Measurements*. in *The Structure and Conformation of Amphiphilic Membranes*. 1992. Berlin, Heidelberg: Springer Berlin Heidelberg.
25. Hermann, E., et al., *Automated analysis of giant unilamellar vesicles using circular Hough transformation.* Bioinformatics, 2014. **30**(12): p. 1747-54.
26. Toth, D.J., et al., *Acute depletion of plasma membrane phosphatidylinositol 4,5-bisphosphate impairs specific steps in endocytosis of the G-protein-coupled receptor.* J Cell Sci, 2012. **125**(Pt 9): p. 2185-97.
27. Schindelin, J., et al., *Fiji: an open-source platform for biological-image analysis.* Nature Methods, 2012. **9**(7): p. 676-682.
28. Heuser, J., *The production of 'cell cortices' for light and electron microscopy.* Traffic, 2000. **1**(7): p. 545-552.
29. Garton, M., et al., *Method to generate highly stable D-amino acid analogs of bioactive helical peptides using a mirror image of the entire PDB.* Proc of the Natl Acad of Sci USA, 2018. **115**(7): p. 1505-1510.
30. Jorgensen, W.L., et al., *Comparison of simple potential functions for simulating liquid water.* J Chemi Phys, 1983. **79**(2): p. 926-935.
31. Jo, S., et al., *CHARMM-GUI: a web-based graphical user interface for CHARMM.* J Comput Chem, 2008. **29**(11): p. 1859-1865.
32. Jo, S., T. Kim, and W. Im, *Automated builder and database of protein/membrane complexes for molecular dynamics simulations.* PLoS One, 2007. **2**(9): p. e880.
33. Lee, J., et al., *CHARMM-GUI input generator for NAMD, GROMACS, AMBER, OpenMM, and CHARMM/OpenMM dimulations using the CHARMM36 additive force field.* J Chem Theory Comput, 2016. **12**(1): p. 405-413.
34. Huang, J., et al., *CHARMM36m: an improved force field for folded and intrinsically disordered proteins.* Nature Methods, 2017. **14**(1): p. 71-73.
35. Huang, J. and A.D. MacKerell, Jr., *CHARMM36 all-atom additive protein force field: validation based on comparison to NMR data.* J of Comput Chem, 2013. **34**(25): p. 2135-2145.
36. Bussi, G., D. Donadio, and M. Parrinello, *Canonical sampling through velocity rescaling.* J Chem Phys, 2007. **126**(1): p. 014101.
37. Berendsen, H.J.C., et al., *Molecular dynamics with coupling to an external bath.* J Chem Phys, 1984. **81**(8): p. 3684-3690.
38. Evans, D.J. and B.L. Holian, *The Nose–Hoover thermostat.* J Chem Phys, 1985. **83**(8): p. 4069-4074.
39. Essmann, U., et al., *A smooth particle mesh Ewald method.* J Chem Phys, 1995. **103**(19): p. 8577-8593.
40. Johnson, J.K., J.A. Zollweg, and K.E. Gubbins, *The Lennard-Jones equation of state revisited.* Mol Phys, 1993. **78**(3): p. 591-618.
41. Humphrey, W., A. Dalke, and K. Schulten, *VMD: Visual molecular dynamics.* J Mol Graph, 1996. **14**(1): p. 33-38.
42. Abraham, M.J., et al., *GROMACS: High performance molecular simulations through multi-level parallelism from laptops to supercomputers.* SoftwareX, 2015. **1-2**: p. 19-25.
43. Kutzner, C., et al., *More bang for your buck: Improved use of GPU nodes for GROMACS 2018.* J of Comput Chem, 2019. **40**(27): p. 2418-2431.
44. Ingolfsson, H.I., et al., *Lipid organization of the plasma membrane.* J Am Chem Soc, 2014. **136**(41): p. 14554-9.
45. Wang, Y., et al., *2A self-cleaving peptide-based multi-gene expression system in the silkworm Bombyx mori.* Sci Rep, 2015. **5**: p. 16273.

46. Suh, B.-C., et al., *Rapid chemically induced changes of PtdIns(4,5)P_2 gate KCNQ ion channels.* Science, 2006. **314**(5804): p. 1454-1457.
47. Raucher, D., et al., *Phosphatidylinositol 4,5-bisphosphate functions as a second messenger that regulates cytoskeleton–plasma membrane adhesion.* Cell, 2000. **100**(2): p. 221-228.

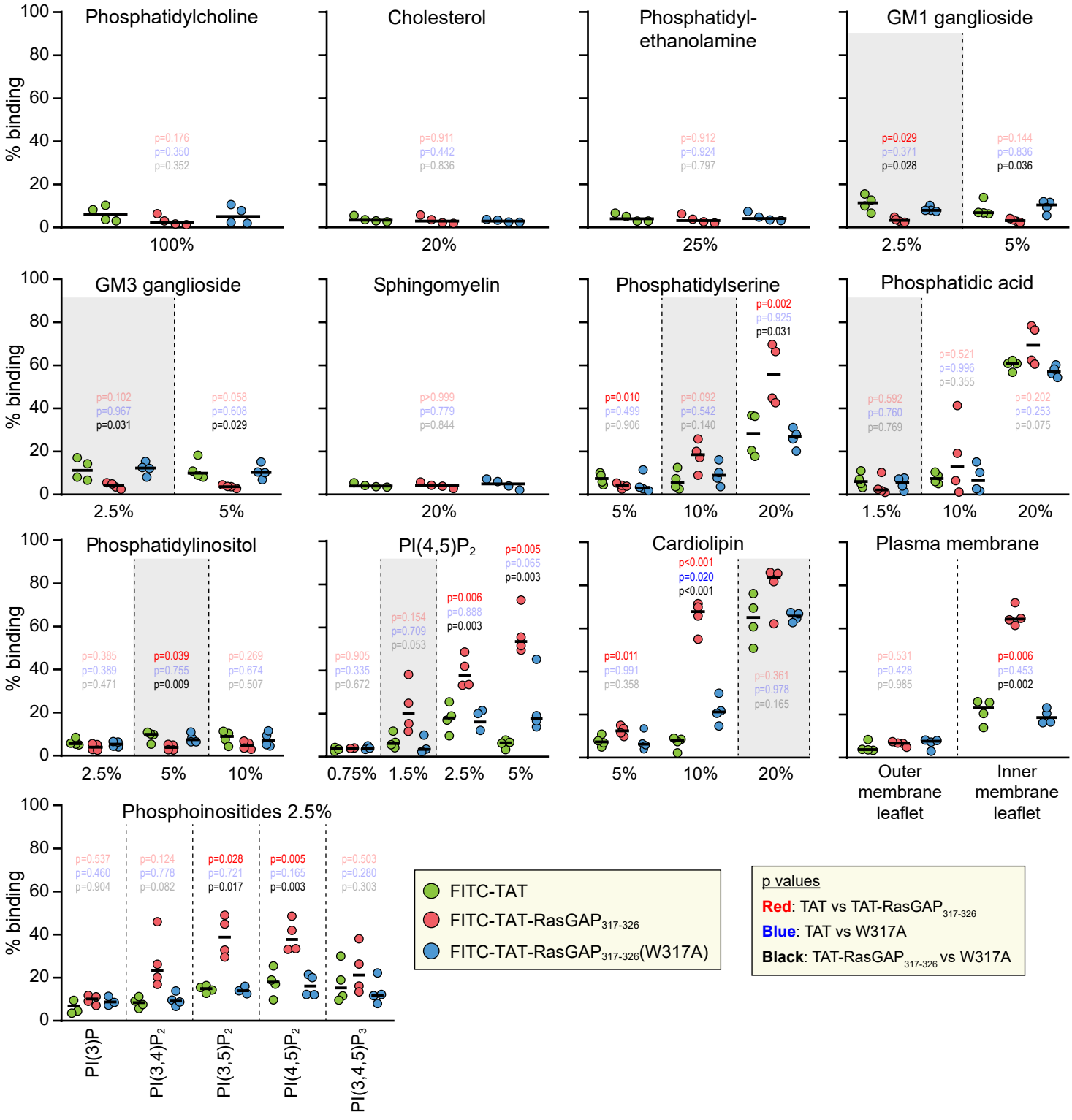
Phosphatidylcholine
Cholesterol
Phosphatidyl-ethanolamine
GM1 ganglioside
GM3 ganglioside
Sphingomyelin
Phosphatidylserine
Phosphatidic acid
Phosphatidylinositol
PI(4,5)P2
Cardiolipin
Plasma membrane
Phosphoinositides 2.5%
% binding
100%
20%
25%
2.5%
5%
1.5%
10%
20%
0.75%
1.5%
2.5%
Outer membrane leaflet
Inner membrane leaflet
PI(3)P
PI(3,4)P2
PI(3,5)P2
PI(4,5)P2
PI(3,4,5)P3
FITC-TAT
FITC-TAT-RasGAP317-326
FITC-TAT-RasGAP317-326(W317A)
p values
Red: TAT vs TAT-RasGAP317-326
Blue: TAT vs W317A
Black: TAT-RasGAP317-326 vs W317A

Figure 1

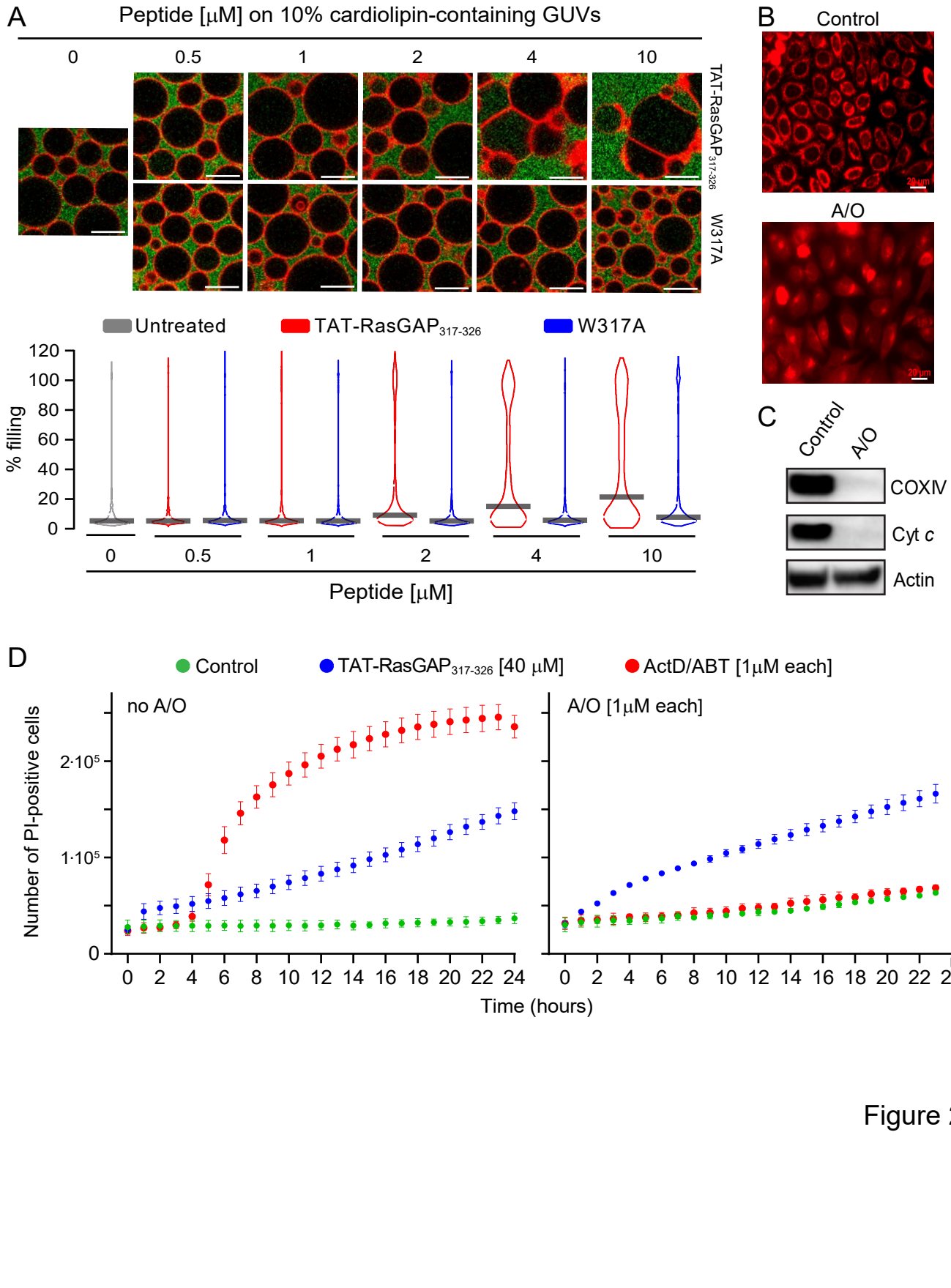
A
Peptide [μM] on 10% cardiolipin-containing GUVs
0
0.5
1
2
4
10
TAT-RasGAP317-326
W317A
Untreated
TAT-RasGAP317-326
W317A
% filling
120
100
80
60
40
20
0
0
0.5
1
2
4
10
Peptide [μM]
B
Control
20 μm
A/O
20 μm
C
Control
A/O
COXIV
Cyt c
Actin
D
Control
TAT-RasGAP317-326 [40 μM]
ActD/ABT [1μM each]
no A/O
A/O [1μM each]
Number of PI-positive cells
2·10⁵
1·10⁵
0
0 2 4 6 8 10 12 14 16 18 20 22 24
Time (hours)

Figure 2

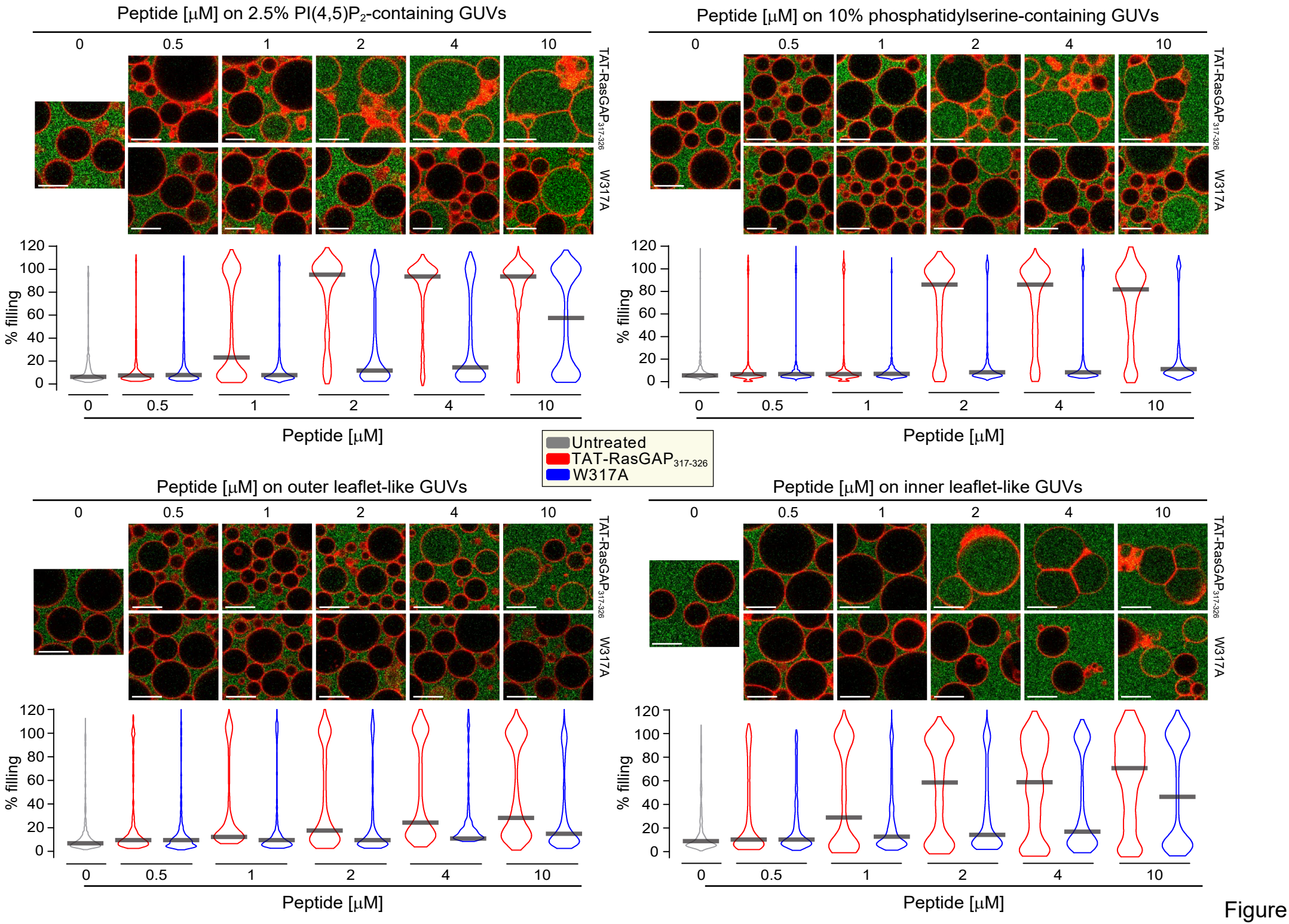
Peptide [μM] on 2.5% PI(4,5)P2-containing GUVs
Peptide [μM] on 10% phosphatidylserine-containing GUVs
Peptide [μM] on outer leaflet-like GUVs
Peptide [μM] on inner leaflet-like GUVs
0
0.5
1
2
4
10
TAT-RasGAP317-326
W317A
% filling
Peptide [μM]
Untreated
TAT-RasGAP317-326
W317A

Figure 3

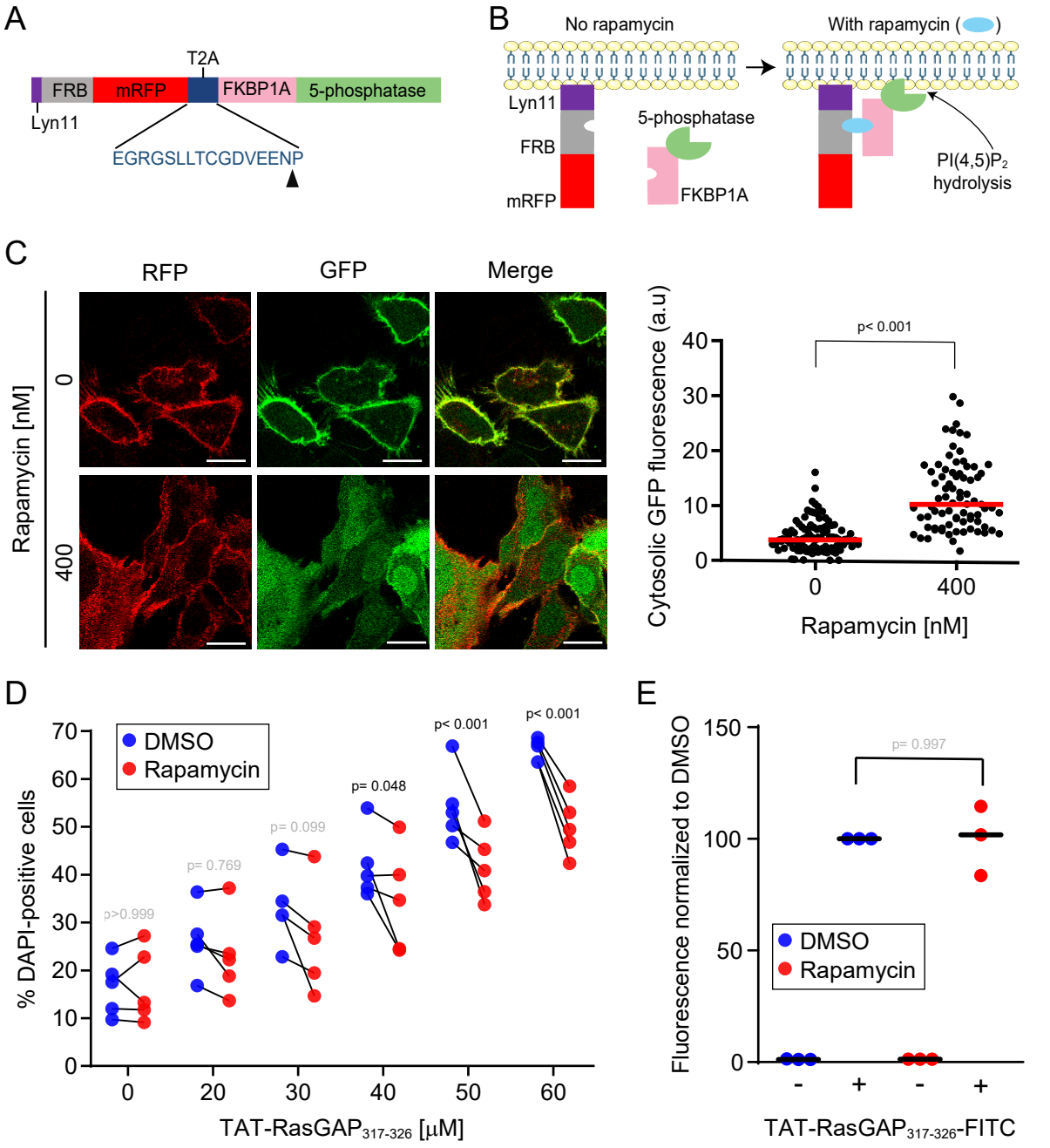
A
T2A
FRB
mRFP
FKBP1A
5-phosphatase
Lyn11
EGRGSLLTCGDVEENP
B
No rapamycin
With rapamycin ( )
Lyn11
FRB
mRFP
5-phosphatase
FKBP1A
PI(4,5)P2
hydrolysis
C
RFP
GFP
Merge
Rapamycin [nM]
0
400
Cytosolic GFP fluorescence (a.u)
p< 0.001
Rapamycin [nM]
D
DMSO
Rapamycin
% DAPI-positive cells
p>0.999
p= 0.769
p= 0.099
p= 0.048
p< 0.001
p< 0.001
TAT-RasGAP317-326 [μM]
E
Fluorescence normalized to DMSO
p= 0.997
DMSO
Rapamycin
TAT-RasGAP317-326-FITC

Figure 4

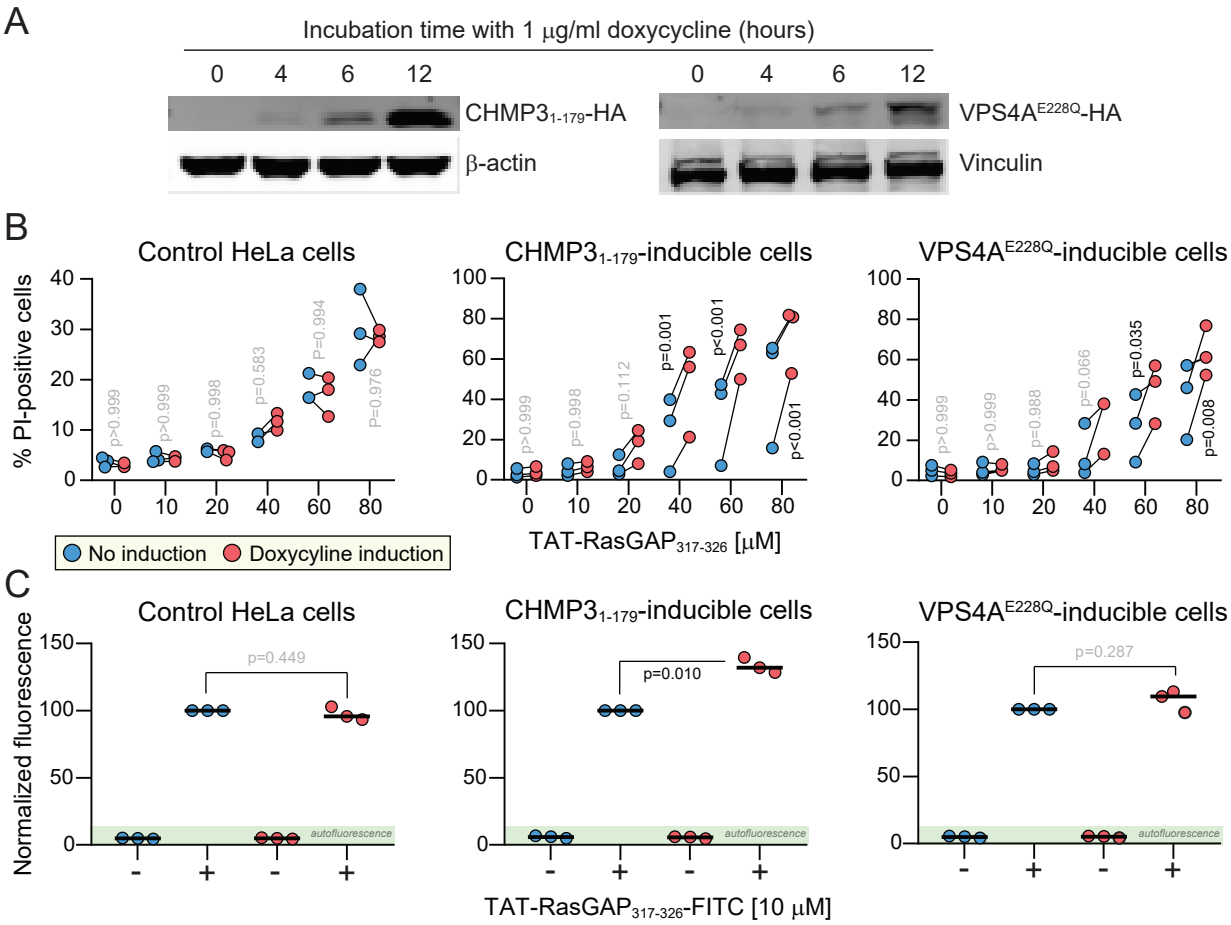
A
Incubation time with 1 μg/ml doxycycline (hours)
0 4 6 12
0 4 6 12
CHMP3$_{1-179}$-HA
β-actin
VPS4A^{E228Q}-HA
Vinculin
B
Control HeLa cells
CHMP3$_{1-179}$-inducible cells
VPS4A^{E228Q}-inducible cells
% PI-positive cells
p>0.999
p>0.999
p=0.998
p=0.583
P=0.994
P=0.976
p>0.999
p=0.998
p=0.112
p=0.001
p<0.001
p<0.001
p>0.999
p>0.999
p=0.988
p=0.066
p=0.035
p=0.008
No induction
Doxycyline induction
TAT-RasGAP$_{317-326}$ [μM]
C
Control HeLa cells
CHMP3$_{1-179}$-inducible cells
VPS4A^{E228Q}-inducible cells
Normalized fluorescence
p=0.449
p=0.010
p=0.287
autofluorescence
TAT-RasGAP$_{317-326}$-FITC [10 μM]

Figure 5

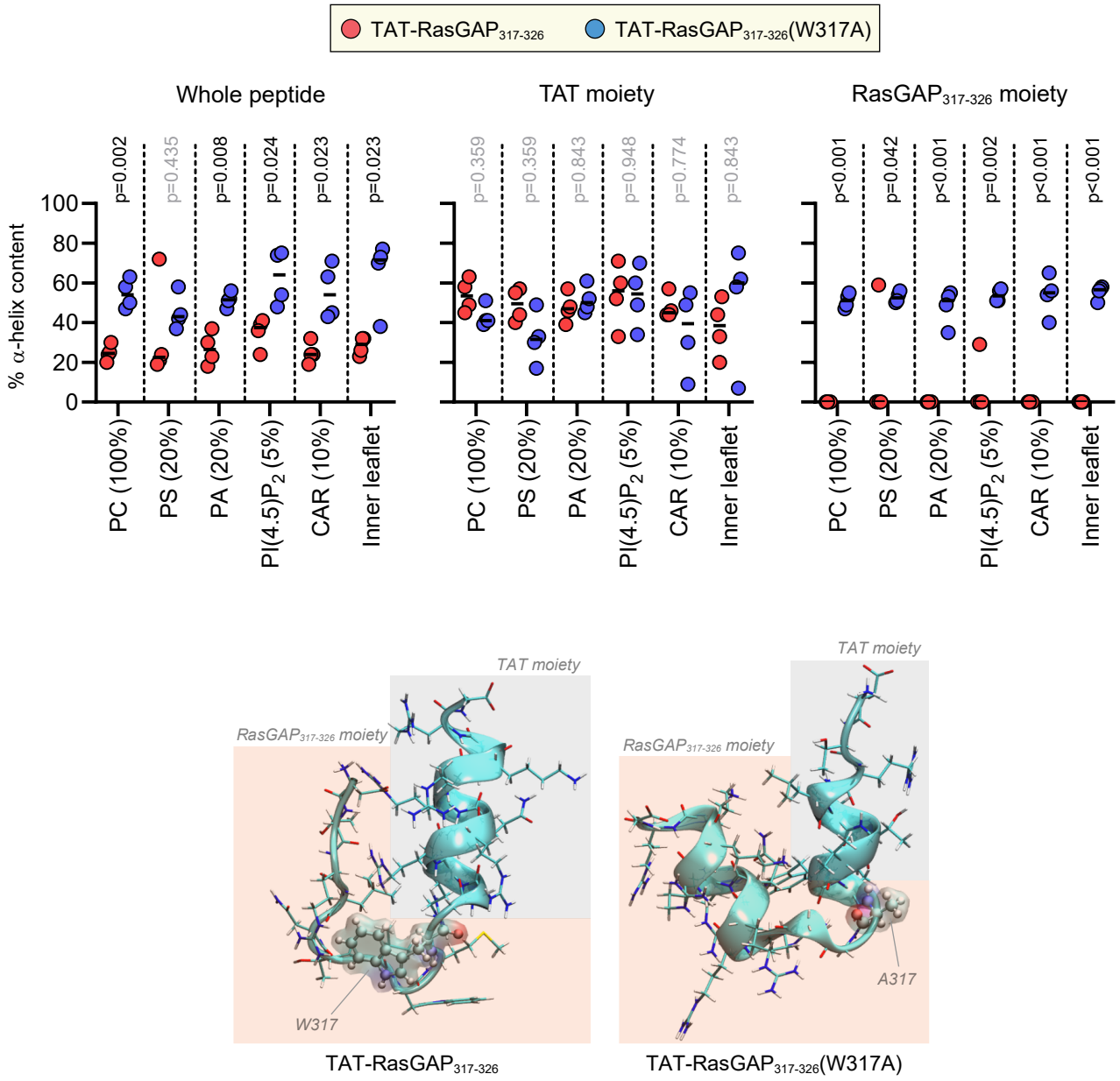
TAT-RasGAP317-326
TAT-RasGAP317-326(W317A)
Whole peptide
TAT moiety
RasGAP317-326 moiety
% α-helix content
100
80
60
40
20
0
p=0.002
p=0.435
p=0.008
p=0.024
p=0.023
p=0.023
p=0.359
p=0.359
p=0.843
p=0.948
p=0.774
p=0.843
p<0.001
p=0.042
p<0.001
p=0.002
p<0.001
p<0.001
PC (100%)
PS (20%)
PA (20%)
PI(4.5)P2 (5%)
CAR (10%)
Inner leaflet
TAT moiety
RasGAP317-326 moiety
W317
TAT-RasGAP317-326
TAT moiety
RasGAP317-326 moiety
A317
TAT-RasGAP317-326(W317A)

Figure 6

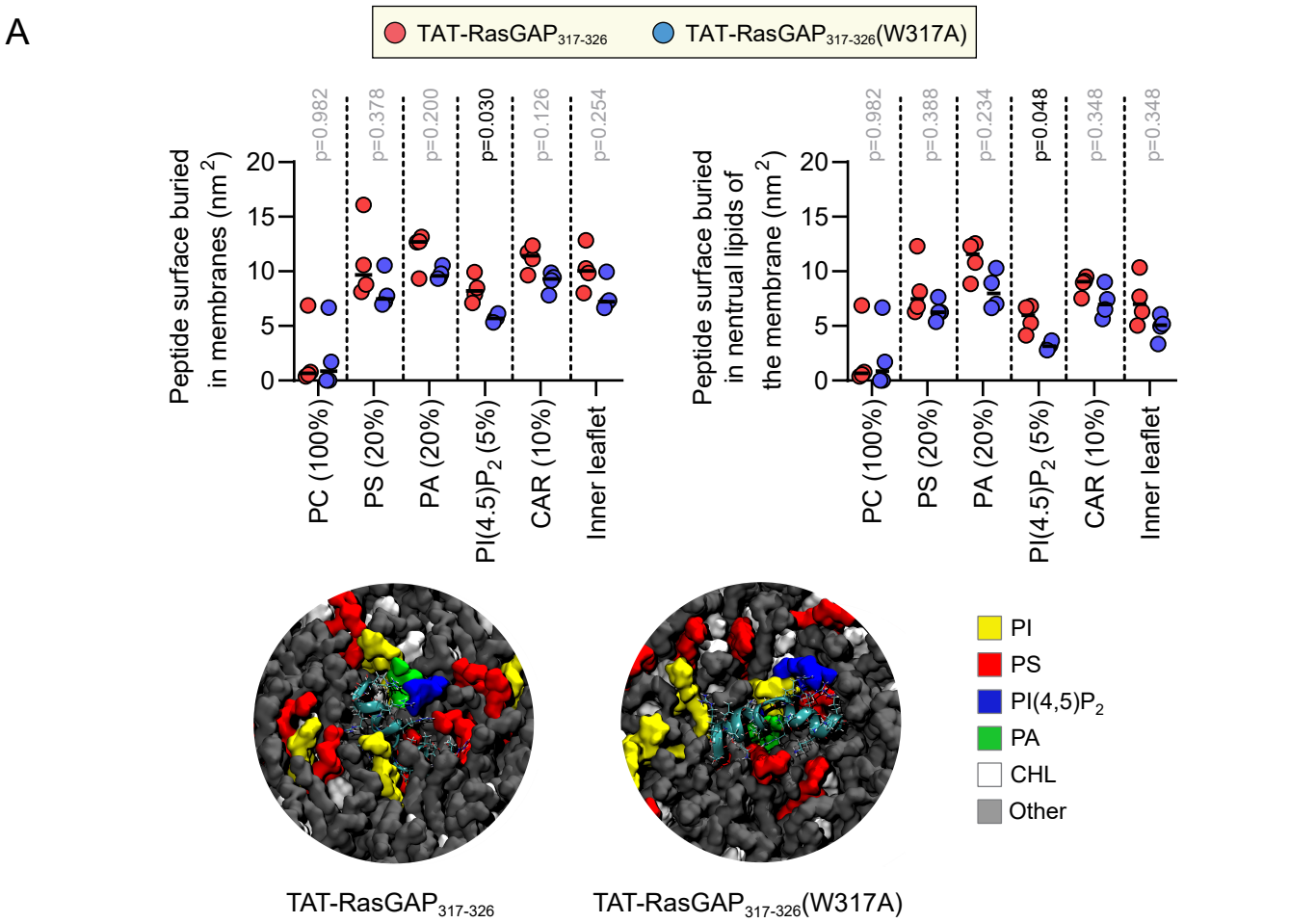
A
TAT-RasGAP317-326
TAT-RasGAP317-326(W317A)
Peptide surface buried in membranes (nm2)
Peptide surface buried in nentrual lipids of the membrane (nm2)
p=0.982
p=0.378
p=0.200
p=0.030
p=0.126
p=0.254
p=0.982
p=0.388
p=0.234
p=0.048
p=0.348
p=0.348
PC (100%)
PS (20%)
PA (20%)
PI(4.5)P2 (5%)
CAR (10%)
Inner leaflet
PI
PS
PI(4,5)P2
PA
CHL
Other
TAT-RasGAP317-326
TAT-RasGAP317-326(W317A)

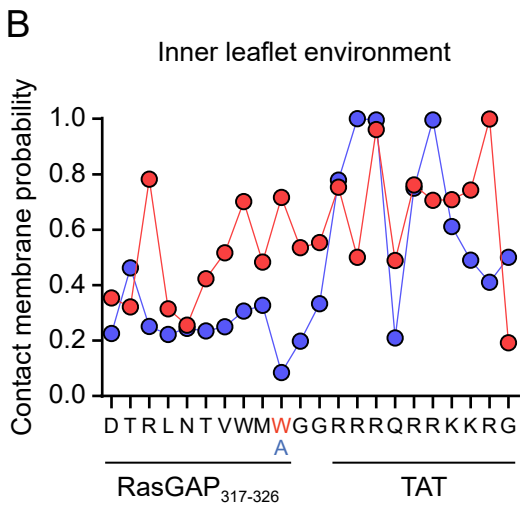
B
Inner leaflet environment
Contact membrane probability
D T R L N T V W M W G G R R R Q R R K K R G
A
RasGAP317-326
TAT

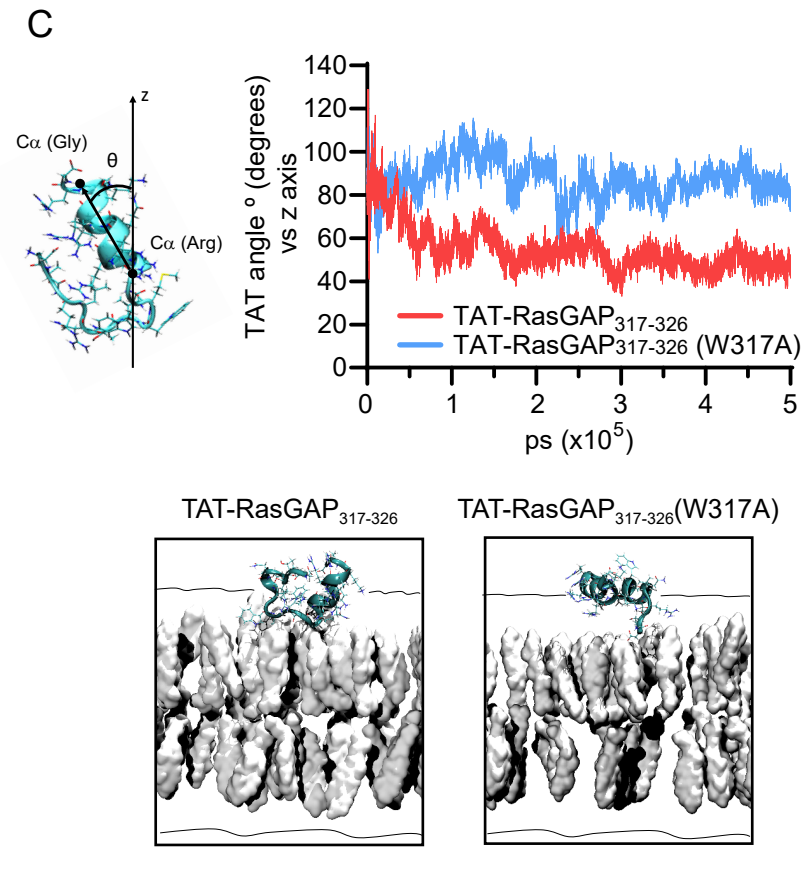
C
Cα (Gly)
θ
Cα (Arg)
z
TAT angle º (degrees) vs z axis
ps (x10^5)
TAT-RasGAP317-326
TAT-RasGAP317-326 (W317A)
TAT-RasGAP317-326
TAT-RasGAP317-326(W317A)

Figure 7

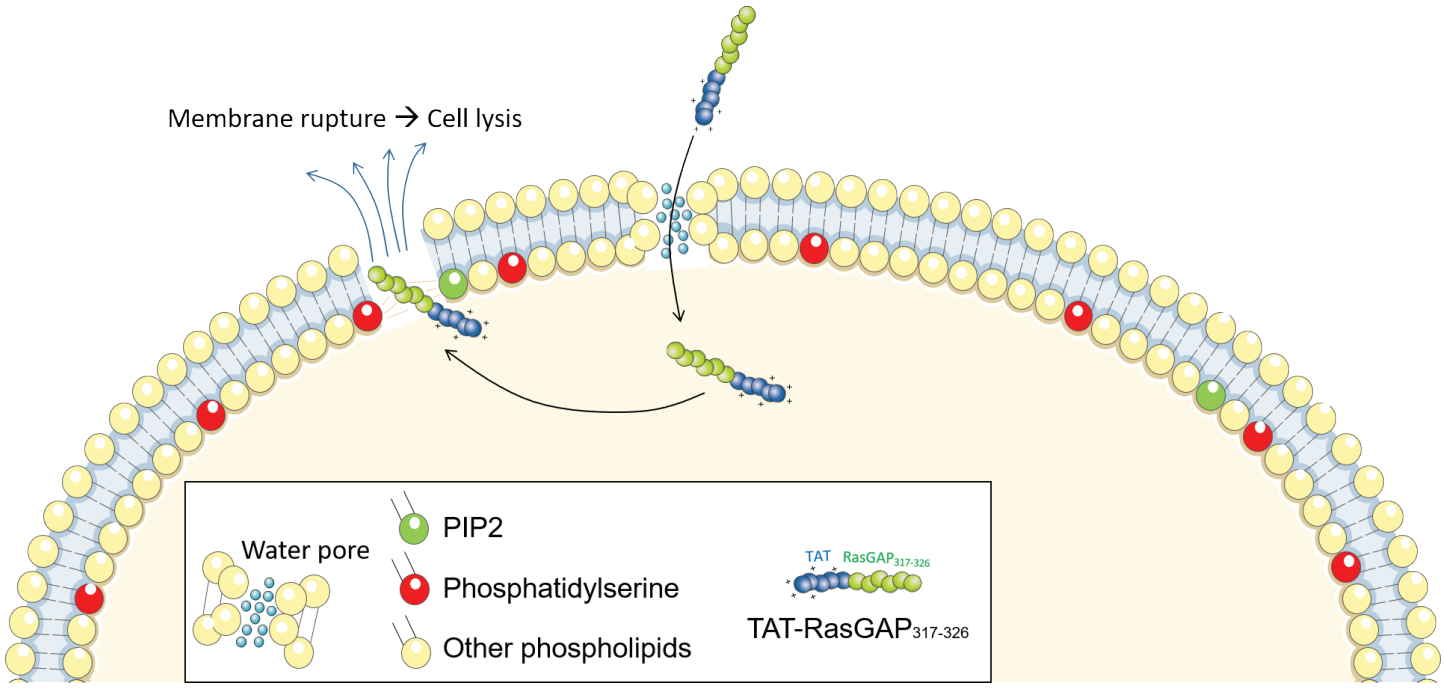
Membrane rupture → Cell lysis
Water pore
PIP2
Phosphatidylserine
Other phospholipids
TAT RasGAP317-326
TAT-RasGAP317-326

Figure 8

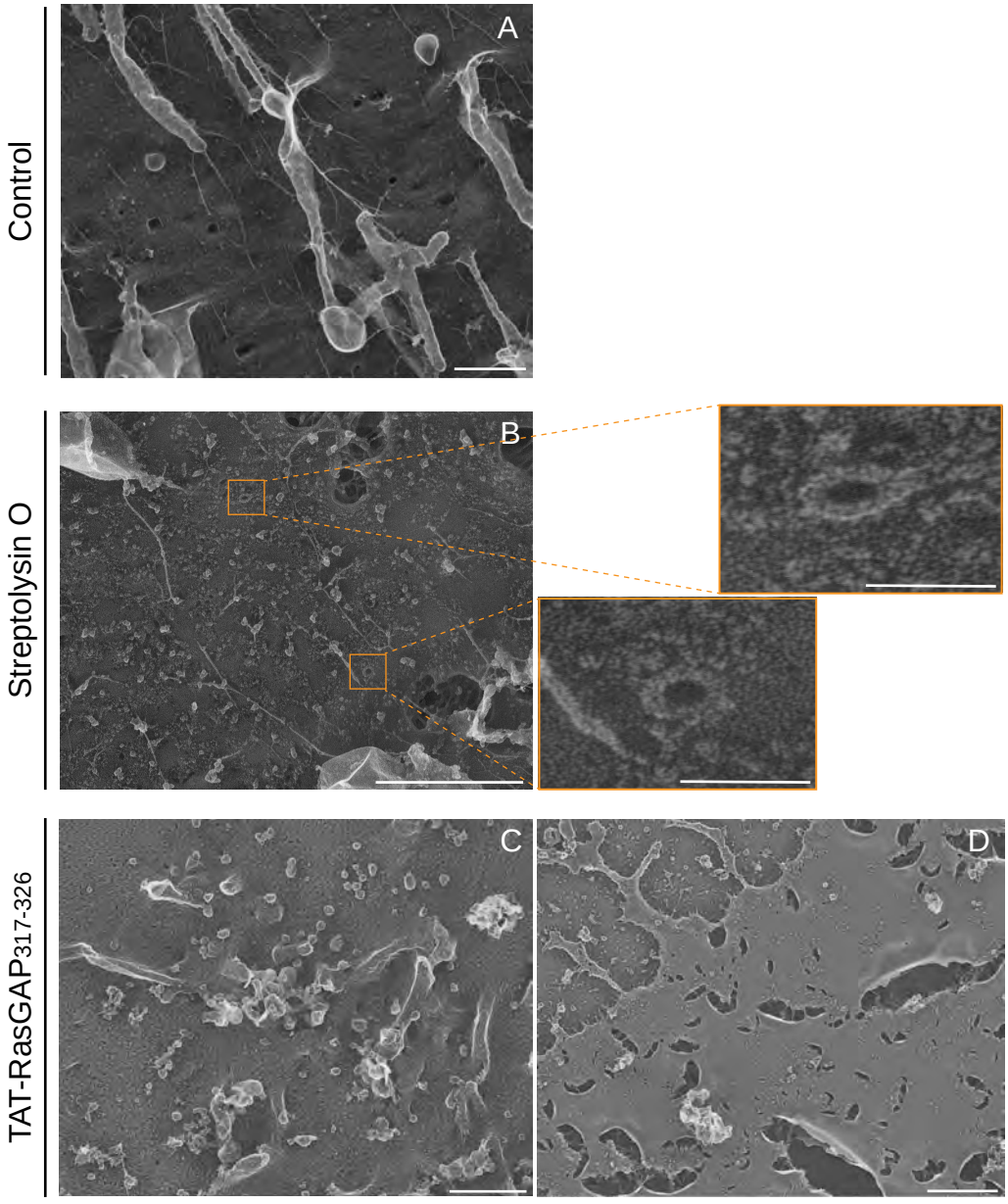
Control
A
Streptolysin O
B
TAT-RasGAP317-326
C
D

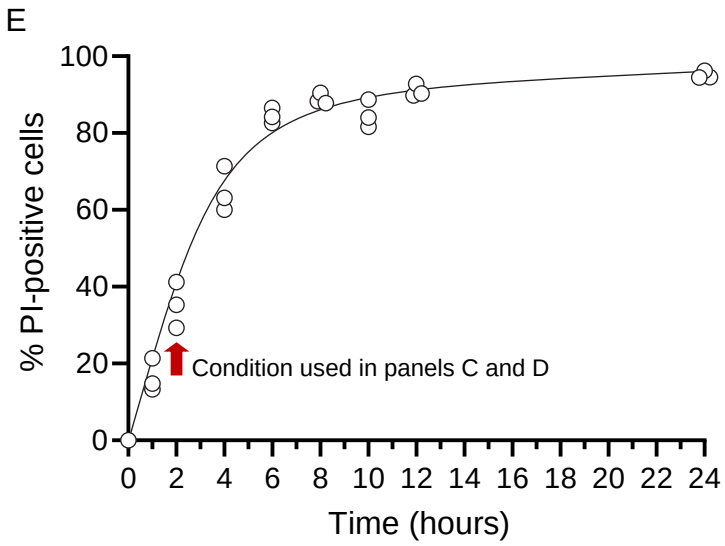
E
% PI-positive cells
100
80
60
40
20
0
Condition used in panels C and D
0 2 4 6 8 10 12 14 16 18 20 22 24
Time (hours)

Figure S1

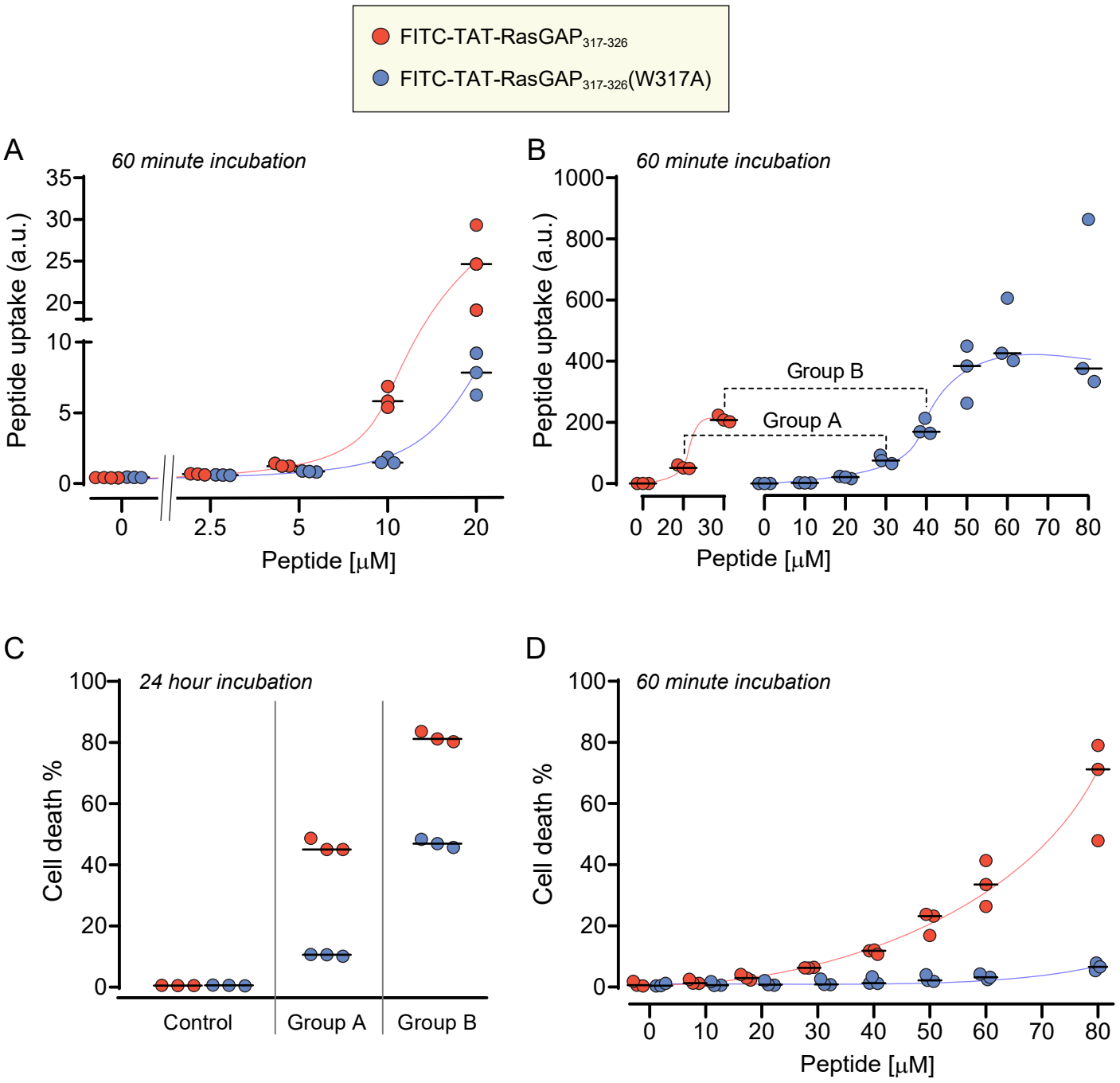
FITC-TAT-RasGAP317-326
FITC-TAT-RasGAP317-326(W317A)
A
60 minute incubation
Peptide uptake (a.u.)
Peptide [μM]
B
60 minute incubation
Peptide uptake (a.u.)
Group B
Group A
Peptide [μM]
C
24 hour incubation
Cell death %
Control
Group A
Group B
D
60 minute incubation
Cell death %
Peptide [μM]

Figure S2

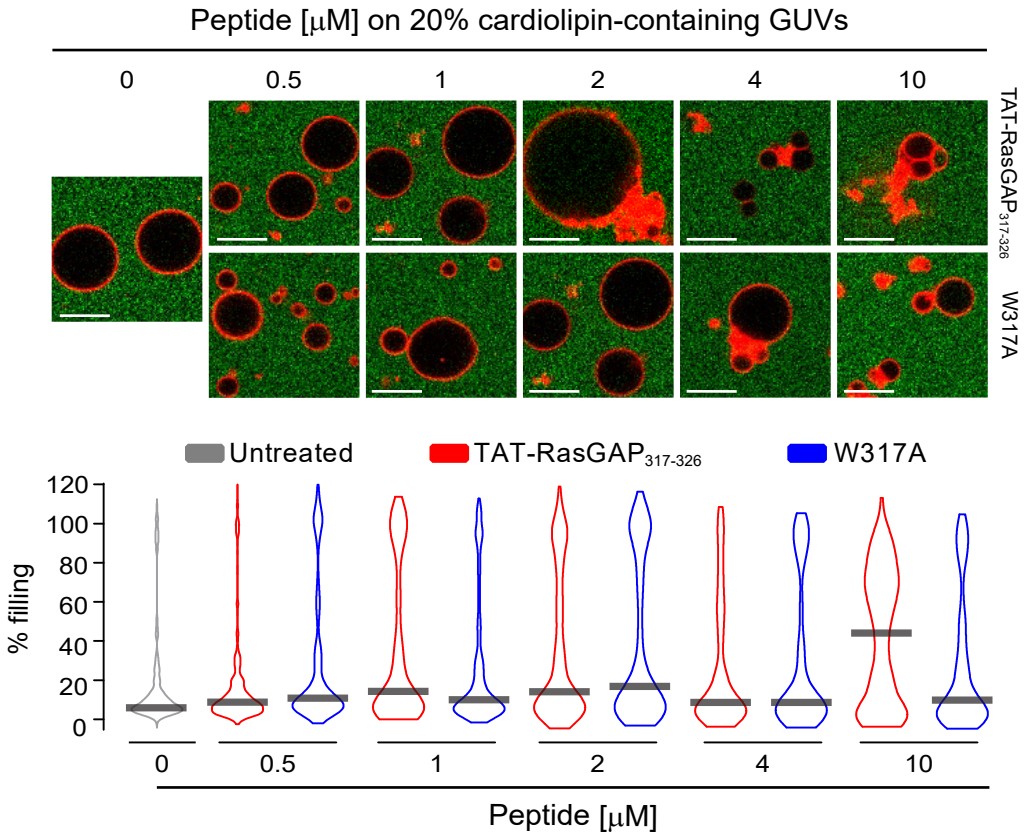
Peptide [μM] on 20% cardiolipin-containing GUVs
0
0.5
1
2
4
10
TAT-RasGAP317-326
W317A
Untreated
TAT-RasGAP317-326
W317A
% filling
120
100
80
60
40
20
0
0
0.5
1
2
4
10
Peptide [μM]

Figure S3

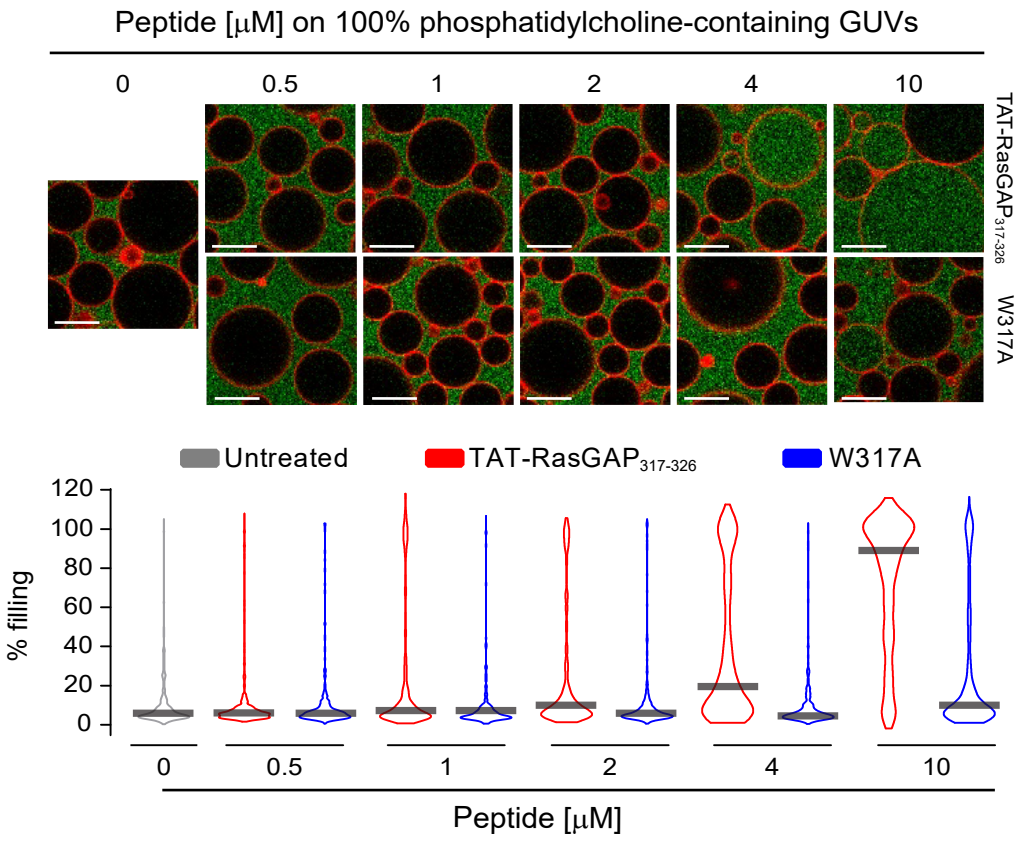
Peptide [μM] on 100% phosphatidylcholine-containing GUVs
0
0.5
1
2
4
10
TAT-RasGAP317-326
W317A
Untreated
TAT-RasGAP317-326
W317A
% filling
120
100
80
60
40
20
0
0
0.5
1
2
4
10
Peptide [μM]

Figure S4

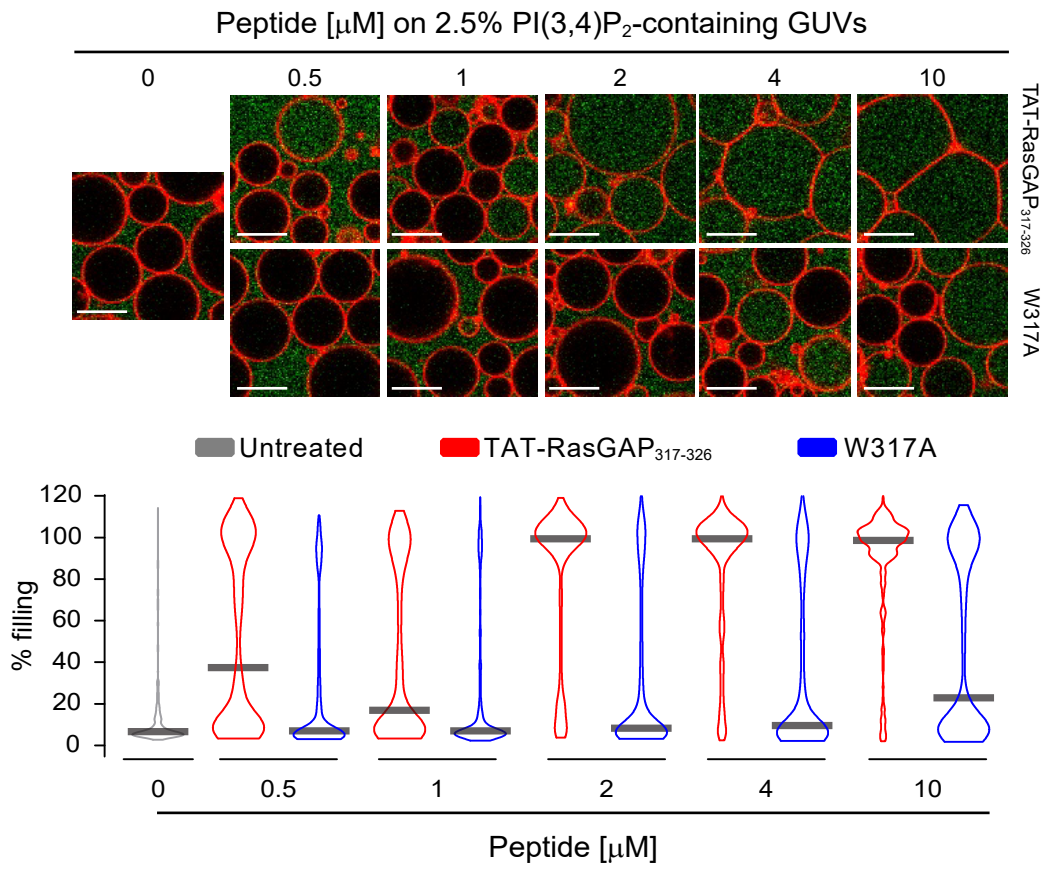
Peptide [μM] on 2.5% PI(3,4)P2-containing GUVs
0
0.5
1
2
4
10
TAT-RasGAP317-326
W317A
Untreated
TAT-RasGAP317-326
W317A
% filling
120
100
80
60
40
20
0
Peptide [μM]

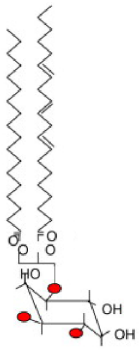
PI(3,4)P2

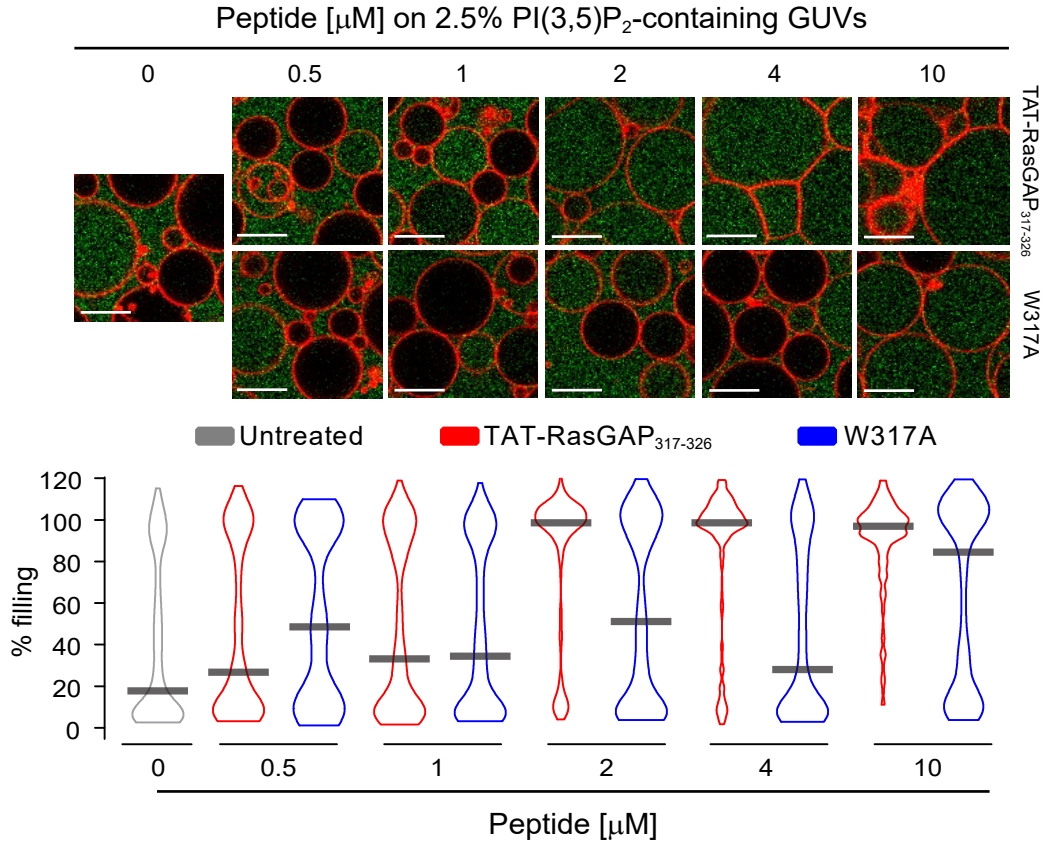
Peptide [μM] on 2.5% PI(3,5)P2-containing GUVs
0
0.5
1
2
4
10
TAT-RasGAP317-326
W317A
Untreated
TAT-RasGAP317-326
W317A
% filling
120
100
80
60
40
20
0
Peptide [μM]

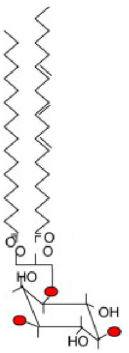
PI(3,5)P2

Figure S5

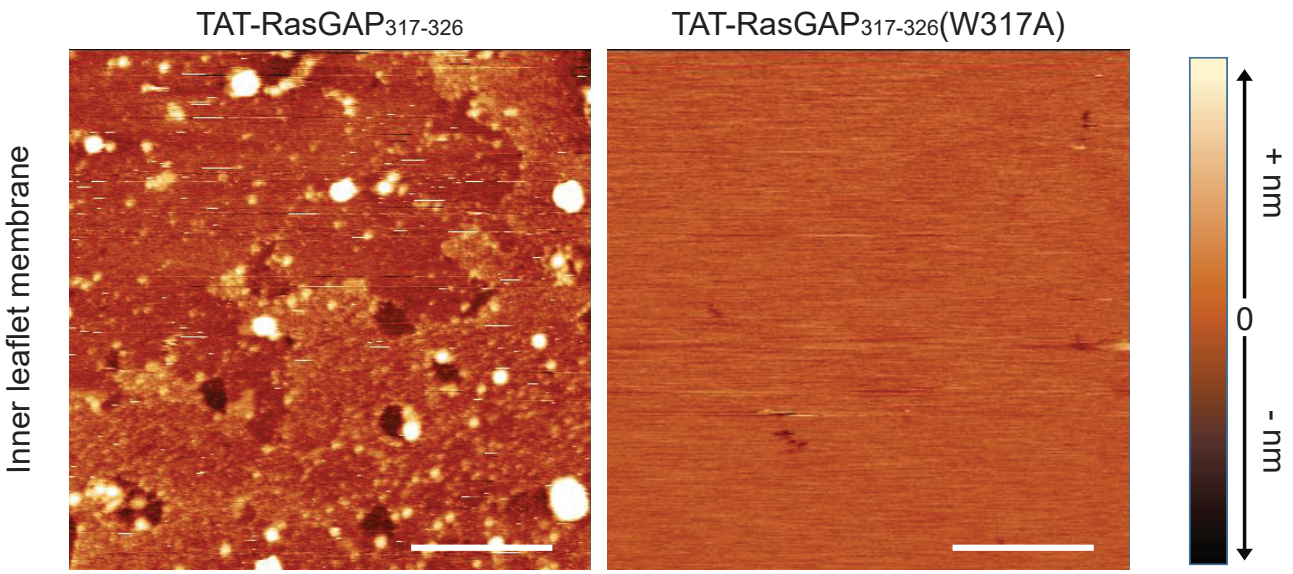
TAT-RasGAP317-326
TAT-RasGAP317-326(W317A)
Inner leaflet membrane
+ nm
0
- nm

Figure S6

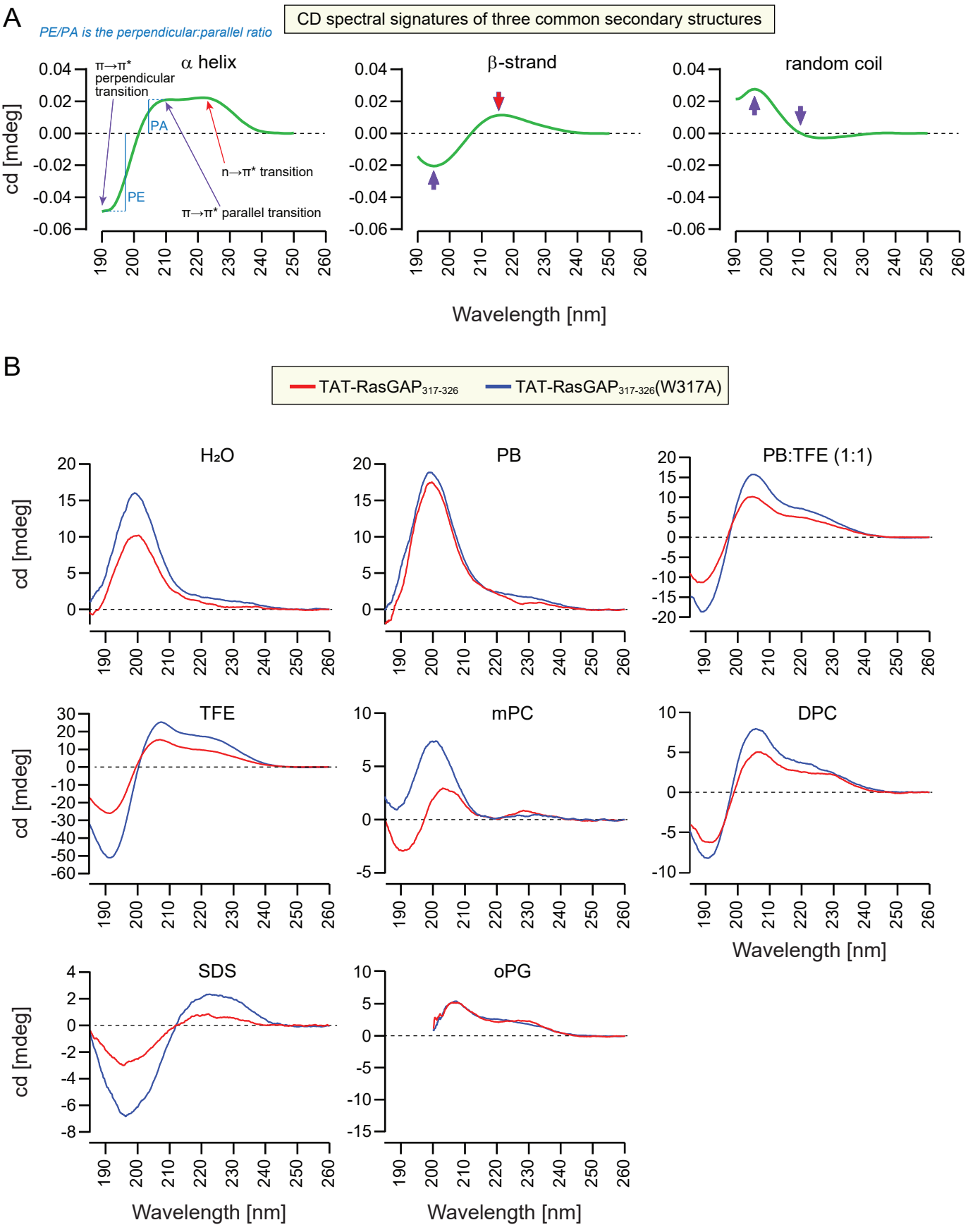
A
PE/PA is the perpendicular:parallel ratio
CD spectral signatures of three common secondary structures
α helix
β-strand
random coil
π→π* perpendicular transition
PA
PE
n→π* transition
π→π* parallel transition
cd [mdeg]
Wavelength [nm]
B
TAT-RasGAP317-326
TAT-RasGAP317-326(W317A)
H2O
PB
PB:TFE (1:1)
TFE
mPC
DPC
SDS
oPG
cd [mdeg]
Wavelength [nm]

Figure S7

A

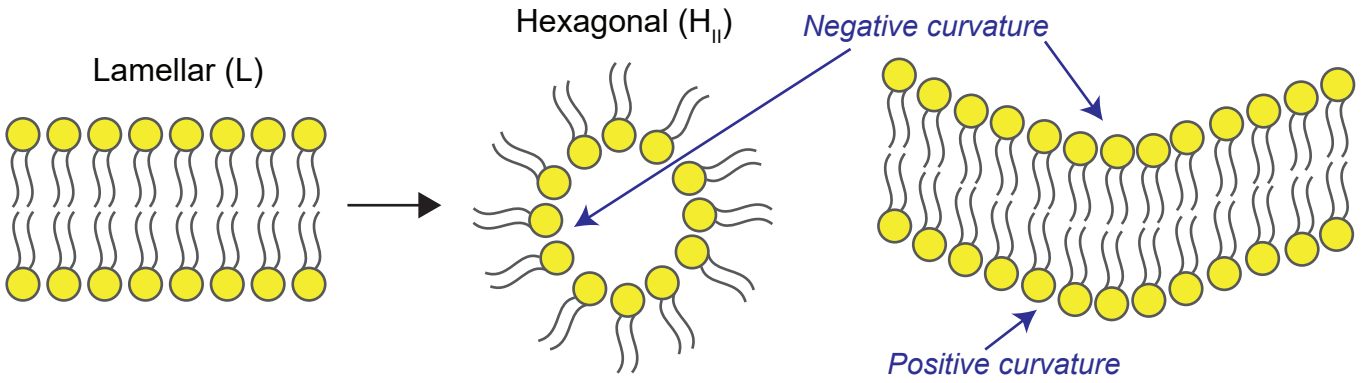
Lamellar (L)
Hexagonal (H_{II})
Negative curvature
Positive curvature

B

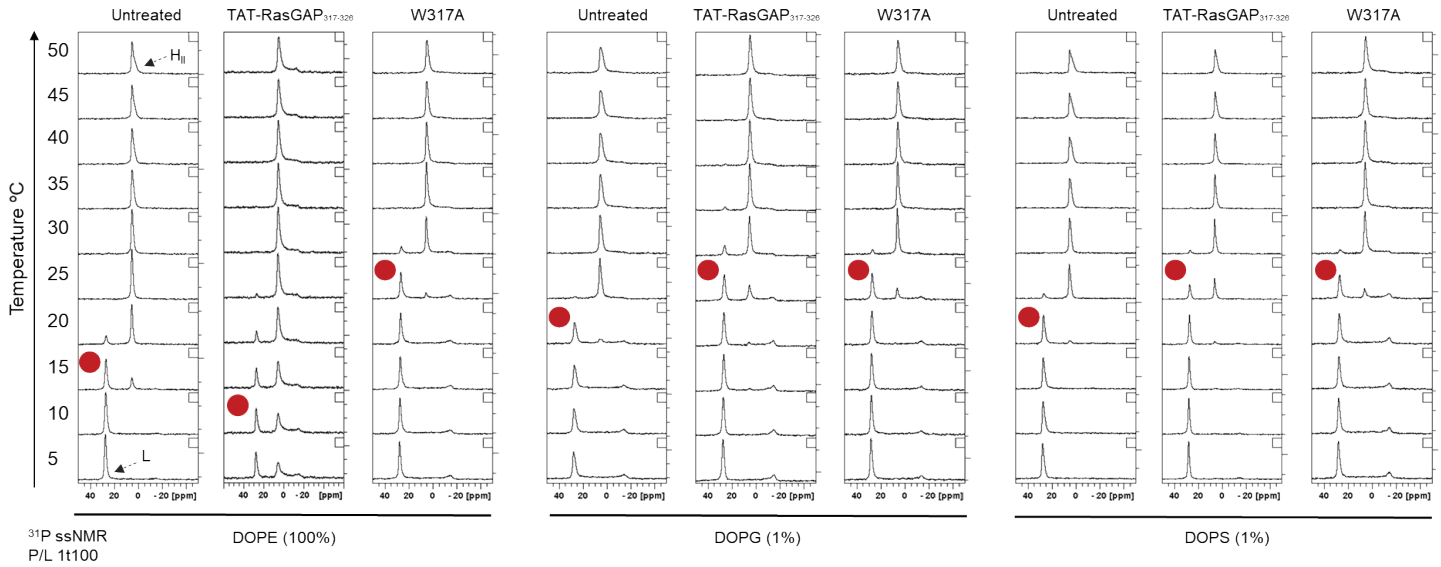
Untreated
TAT-RasGAP317-326
W317A
Temperature °C
50
45
40
35
30
25
20
15
10
5
H_{II}
L
40 20 0 -20 [ppm]
^{31}P ssNMR
P/L 1t100
DOPE (100%)
DOPG (1%)
DOPS (1%)

Figure S8